

José Domingos Albuquerque Aguiar

**Characterization of soil microstructure
using 3D X-ray tomographic images**

Recife – PE

July 2023



UNIVERSIDADE FEDERAL RURAL DE PERNAMBUCO
PRÓ-REITORIA DE PESQUISA E PÓS-GRADUAÇÃO
PROGRAMA DE PÓS-GRADUAÇÃO EM BIOMETRIA E ESTATÍSTICA APLICADA

Characterization of soil microstructure using 3D X-ray tomographic images

This thesis was considered appropriate for obtaining the title of Ph.D. in **Biometria e Estatística Aplicada**, defended and unanimously approved on 03/07/2023 by the examining committee.

Concentration Area: **Modelagem e métodos computacionais.**

Advisor: **Ph.D. Borko Stosic**
Co-advisor: **Ph.D. Tatijana Stosic**

Recife – PE

July 2023

Dados Internacionais de Catalogação na Publicação
Universidade Federal Rural de Pernambuco
Sistema Integrado de Bibliotecas
Gerada automaticamente, mediante os dados fornecidos pelo(a) autor(a)

A283c Aguiar, José Domingos Albuquerque
Characterization of soil microstructure using 3D X-ray tomographic images / José Domingos
Albuquerque Aguiar. - 2023.
64 f. : il.

Orientador: Borko Stosic.
Coorientadora: Tatijana Stosic.
Inclui referências.

Tese (Doutorado) - Universidade Federal Rural de Pernambuco, Programa de Pós-Graduação em
Biometria e Estatística Aplicada, Recife, 2023.

1. X-Ray CT Scan Soil Samples. 2. Detrended Fluctuation Analysis. 3. Fisher-Shannon plane. 4.
Complexity. 5. Land use change. I. Stosic, Borko, orient. II. Stosic, Tatijana, coorient. III. Título

CDD 519.5

UNIVERSIDADE FEDERAL RURAL DE PERNAMBUCO
PRÓ-REITORIA DE PESQUISA E PÓS-GRADUAÇÃO
PROGRAMA DE PÓS-GRADUAÇÃO EM BIOMETRIA E ESTATÍSTICA APLICADA

Characterization of soil microstructure using 3D X-ray tomographic images

José Domingos Albuquerque Aguiar

This thesis was considered appropriate for obtaining the title of Ph.D. in Biometria e Estatística Aplicada, defended and unanimously approved on 03/07/2023 by the examining committee.

Advisor:

Ph.D. Borko Stosic
UFRPE – Department of Statistics and Informatics

Examining Committee:

Ph.D. Ana Maria Tarquis Alfonso
Polytechnic University of Madrid

Ph.D. Antonio Celso Dantas Antonino
UFPE – Department of Nuclear Energy

Ph.D. Rômulo Simões Cezar Menezes
UFPE – Department of Nuclear Energy

Ph.D. Lucian Bogdan Bejan
UFRPE – Department of Statistics and Informatics

*I dedicate this work to my
parents for having invested in my
education that made me get this far.*

Acknowledgments

To God for the gift of life.

To my father Domingos (in memoriam), who was an example of an honest man who always valued education and for being the foundation of the man I am today.

To my mother Socorro, the strongest woman I've known, for all the care, dedication, education, and love.

To the gifts from God given to me, my children José Domingos Filho and Maria Letícia, for being my greatest motivation.

To my dear wife Polyana, for the love, dedication, patience, and for encouraging me in the pursuit of my goals.

To my sister Amanda, for the supportive conversations that have always helped me.

To my academic parents, professors Borko Stosic and Tatijana Stosic, for all the encouragement and learning. You are examples of professors and researchers.

To UFRPE, for providing all the necessary conditions for the completion of this work.

To PPGBEA for the welcoming of its professors, students, and staff.

To the Department of Nuclear Energy at UFPE for supporting and assisting this research.

To IFPE, which made the completion of this work possible.

To the members of the defense committee for their contributions to this work.

To the CAPES and CNPq programs for encouraging research in Brazil.

To all the friends who directly or indirectly contributed to this journey of mine, especially to my great friend Edgo for all the guidance during the course.

Thank you.

*“Perseverance is not a long race;
it is many short races one after
the other.”*

Walter Elliot

Abstract

Dozens of definitions of soil can be found in literature, ranging from the most straightforward concepts, where it is asserted, for example, that soil is a heterogeneous mixture of air, water, inorganic and organic solids, and microorganisms, to more complex concepts, where the soil is considered a living, four-dimensional natural Entity. However, regardless of the adopted definition, the importance of soil is unquestionable, as it provides nutrients for plant growth essential for human and animal nutrition. Moreover, history has frequently shown that its misuse can lead to poverty, hunger, drought, and ecological and economic disasters. This great importance given to soil generates a need for ongoing studies searching for methods and tools that contribute to new knowledge. A powerful tool that can observe the elements of soil in a non-destructive way is computed tomography (CT). Despite advances in the resolution of CT equipment and computer power, there is no consensus on data analysis methods that can reveal the complexity of all elements associated with 3D soil images, especially methods that do not require a threshold to segment images. In this context, this work employs two methods originally developed for the analysis of complex signals, Detrended Fluctuation Analysis (DFA) and Fisher-Shannon (FS), to bring a new understanding of the complexity of morphological properties of soil based on the analysis of 3D CT images. Up to date, these two methods have not been used in 3D image analysis. In this work, 3D soil tomographic images were analyzed using DFA in its original form and its generalization for 2D and 3D data. The results of DFA exponents were found to be smaller than 0.5 indicating antipersistence of local density fluctuations, which are consistently stronger (lower exponent value) for the sugar cane plantation sample, than for the Atlantic Forest. Furthermore, a new complexity measure is defined as the distance from the isocomplexity line in the normalized FS plane, which may be seen as a quantifier of soil degradation level. This novel approach resulted in a high grouping success rate (91.7%) between soil covered by native vegetation (Atlantic Forest) and soil that was the subject of the degradation process as the consequence of land use change (from native Atlantic Forest to sugarcane cultivation).

Keywords: X-Ray CT Scan Soil Samples. Detrended Fluctuation Analysis. Fisher-Shannon plane. Complexity. Land use change.

Resumo

Dezenas de definições de solo podem ser encontradas na literatura, desde os conceitos mais simples, onde se afirma, por exemplo, que o solo é uma mistura heterogênea de ar, água, sólidos inorgânicos e orgânicos, e microrganismos, até conceitos mais complexos, onde o solo é considerado uma Entidade natural viva e quadridimensional. No entanto, independentemente da definição adotada, a importância do solo é inquestionável, pois fornece nutrientes para o crescimento vegetal essenciais para a nutrição humana e animal. Além disso, a história tem mostrado frequentemente que seu mau uso pode levar à pobreza, fome, seca e desastres ecológicos e econômicos. Essa grande importância dada ao solo gera a necessidade de estudos contínuos em busca de métodos e ferramentas que contribuam para novos conhecimentos. Uma poderosa ferramenta que pode observar os elementos do solo de forma não destrutiva é a tomografia computadorizada (TC). Apesar dos avanços na resolução dos equipamentos de TC e na potência computacional, não há consenso sobre métodos de análise de dados que possam revelar a complexidade de todos os elementos associados às imagens 3D do solo, especialmente métodos que não necessitam de um limiar para segmentar imagens. Neste contexto, este trabalho emprega dois métodos originalmente desenvolvidos para a análise de sinais complexos, a Análise de Flutuação Destendenciada (DFA) e Fisher-Shannon (FS), para trazer uma nova compreensão da complexidade das propriedades morfológicas do solo com base na análise de imagens 3D de TC. Até o presente momento, esses dois métodos não foram utilizados na análise de imagens 3D. Neste trabalho, foram analisadas imagens tomográficas de solo 3D utilizando DFA em sua forma original e sua generalização para dados 2D e 3D. Os resultados dos expoentes da DFA foram menores que 0,5, indicando antipersistência das flutuações da densidade local, que são consistentemente mais fortes (menor valor do expoente) para a amostra do canal do que para a Mata Atlântica. Além disso, uma nova medida de complexidade é definida como a distância da linha de isocomplexidade no plano normalizado do FS, que pode ser vista como um quantificador do nível de degradação do solo. Essa nova abordagem resultou em uma alta taxa de sucesso de agrupamento (91,7%) entre o solo coberto por vegetação nativa (Mata Atlântica) e o solo que foi objeto de processo de degradação como consequência da mudança de uso da terra (de Mata Atlântica nativa para o cultivo de cana-de-açúcar).

Palavras-chave: TC por raios X de amostras de solo. Análise de flutuação sem tendência. Plano de Fisher-Shannon. Complexidade. Mudança de uso do solo.

Figure list

CHAPTER 1

- Figure 1.** Four examples of 2D images (790x790 pixels) from a sugar cane plantation soil sample: (a) slice_001, (b) slice_100, (c) slice_395 and (d) slice_790..... 15
- Figure 2.** 3D representation of a sugar cane plantation soil sample..... 15
- Figure 3.** Publications using the terms "tomography" and "soil" from 1982 to 2022, according to the Scopus database..... 16

CHAPTER 2

- Figure 1.** 1D DFA exponent value histograms for the two samples..... 27
- Figure 2.** Color coded DFA exponent values for a) sugarcane, and b) Atlantic Forest sample. The color coding scheme was chosen to emphasize the contrast among the samples, with bounds corresponding to ± 1.5 standard deviations of the composite sample, from the composite mean..... 28
- Figure 3.** 2D DFA exponent value histograms for the two samples..... 29
- Figure 4.** 2D DFA exponent values for the two samples, as a function of depth..... 29

CHAPTER 3

- Figure 1.** Spatial distribution of sample sites, two samples were taken at each site, at 10 and 20cm depth..... 36
- Figure 2.** Spatial distribution of the I_X values in the horizontal projection plane for each sample. Pixels are colour-coded in blue below two standard deviations from the global average and red for values above two standard deviations. A spectrum of colors is used for values in between, as per the colour bar..... 42
- Figure 3.** Spatial distribution of the N_X values in the horizontal projection plane for each sample. Pixels are colour-coded in blue below two standard deviations from the global average and red for values above two standard deviations. A spectrum of colors is used for values in between, as per the colour bar..... 43
- Figure 4.** Spatial distribution of the C_X values in the horizontal projection plane for each sample. Pixels are colour-coded in blue below two standard deviations from the global average and red for values above two standard deviations. A spectrum of colors is used for values in between, as per the colour bar..... 44
- Figure 5.** a) Scatterplot of the original (N_X, I_X) value pairs, and b) a scatterplot of the normalized values (N'_X, I'_X) , together with projections (N'_{X0}, I'_{X0}) to the closest point on the iso-complexity line..... 45

Figure 6. The distances scatterplot from the iso-complexity line, in the order of samples from south to north	46
Figure 7. Samples SC1_20 with $d=0.0342$ (left), and AF1_10 with $d=0.329$ (right), at a threshold of 1500 Hounsfield units.....	47
Figure 8. Fit to a logistic function. The vertical dashed line represents the threshold $d=0.0952$	48

Table list

CHAPTER 2

Table 1. Descriptive statistics of DFA exponent values for the two samples 27

Table 2. Descriptive statistics of 2D DFA exponent values for the two samples 28

CHAPTER 3

Table 1. Descriptive Statistics of Fisher Information Measure I_x 40

Table 2. Descriptive Statistics of Shannon entropy power N_x 40

Table 3. Descriptive Statistics of Fisher-Shannon complexity C_x 41

Table 4. Complexity (distance from the isocomplexity plane) 46

Supplementary information

Table 1: Characteristics and coordinates of soil samples. 52

Abbreviation list

1D	One-dimensional
2D	Two-dimensional
3D	Three-dimensional
AF	Atlantic Forest
CONAB	Companhia Nacional de Abastecimento
CT	Computed tomography
DFA	Detrended Fluctuation Analysis
FIM	Fisher's information measure
FS	Fisher-Shannon
IBGE	Instituto Brasileiro de Geografia e Estatística
MFDFA	Multifractal Detrended Fluctuation analysis
PDF	Probability density function
SC	Sugarcane
SEP	Shannon Entropy Power

Summary

1. General introduction	14
2. Detrended fluctuation analysis of three-dimensional data: application to soil X-ray CT scans	19
2.1 Abstract.....	19
2.2 Introduction	19
2.3 Methodology	21
2.3.1 Detrended fluctuation analysis (1D DFA)	21
2.3.2 Detrended fluctuation analysis in two dimensions (2D DFA)	22
2.3.3 Detrended fluctuation analysis in three dimensions (3D DFA).....	24
2.3.4 Soil samples	26
2.4 Results and discussion	26
2.5 Conclusions	30
3. Quantifying soil complexity using Fisher-Shannon method on 3D X-ray CT scans	33
3.1 Abstract.....	33
3.2 Introduction	33
3.3 Methodology	36
3.3.1 Soil samples	36
3.3.2 The Fisher-Shannon method	37
3.4 Results and discussion	39
3.5 Conclusions	48
4. Final considerations.....	50
5. Supplementary information	52
References	53

1. General introduction

Dozens of definitions of soil can be found in literature, ranging from the most straightforward concepts, where it is asserted, for example, that soil is a heterogeneous mixture of air, water, inorganic and organic solids, and microorganisms (SPARKS, 2003), to more complex concepts, where the soil is considered a living, four-dimensional natural Entity (HARTEMINK, 2016). However, regardless of the adopted definition, the importance of soil is unquestionable, as it provides nutrients for plant growth essential for human and animal nutrition. Moreover, history has frequently shown that its misuse can lead to poverty, hunger, drought, and ecological and economic disasters (BEZDICEK; PAPENDICK; LAL, 2015). This great importance given to soil generates a need for ongoing studies searching for methods and tools that contribute to new knowledge.

A powerful tool that can observe the elements of an object, including soil, in a non-destructive way (JON *et al.*, 2022) is computed tomography (CT), which uses X-rays and computers to record two-dimensional images of multiple slices of an object (figure 1). These images can be assembled with the aid of a computer to form a three-dimensional image of the scanned object (figure 2). The first recorded use of CT was in the medical field in 1971 with the tomography of a human head (HOUNSFIELD, 1973). The first recorded application of CT in the soil field was in 1982 with the analysis of the density of a soil sample (PETROVIC; SIEBERT; RIEKE, 1982). Although the first use of CT to record soil images is over 40 years old, interest in this research field continues with a growing trend, as can be seen from the graph (figure 3) of articles published using the Scopus database with the search terms "tomography and soil" on April 18th, 2023.

Using CT to scan soil samples provides data that can help understand some problems, such as degradation caused by changes in land use. In Brazil, a typical example of this problem occurs in the country's northeastern region with the conversion of areas of the Atlantic Forest biome into areas for sugarcane cultivation. Such conversion can negatively affect soil functions such as water storage and filtration, nutrient storage and recycling, carbon storage, and habitat for biological activity (RABOT *et al.*, 2018), directly influencing associated ecosystem services.

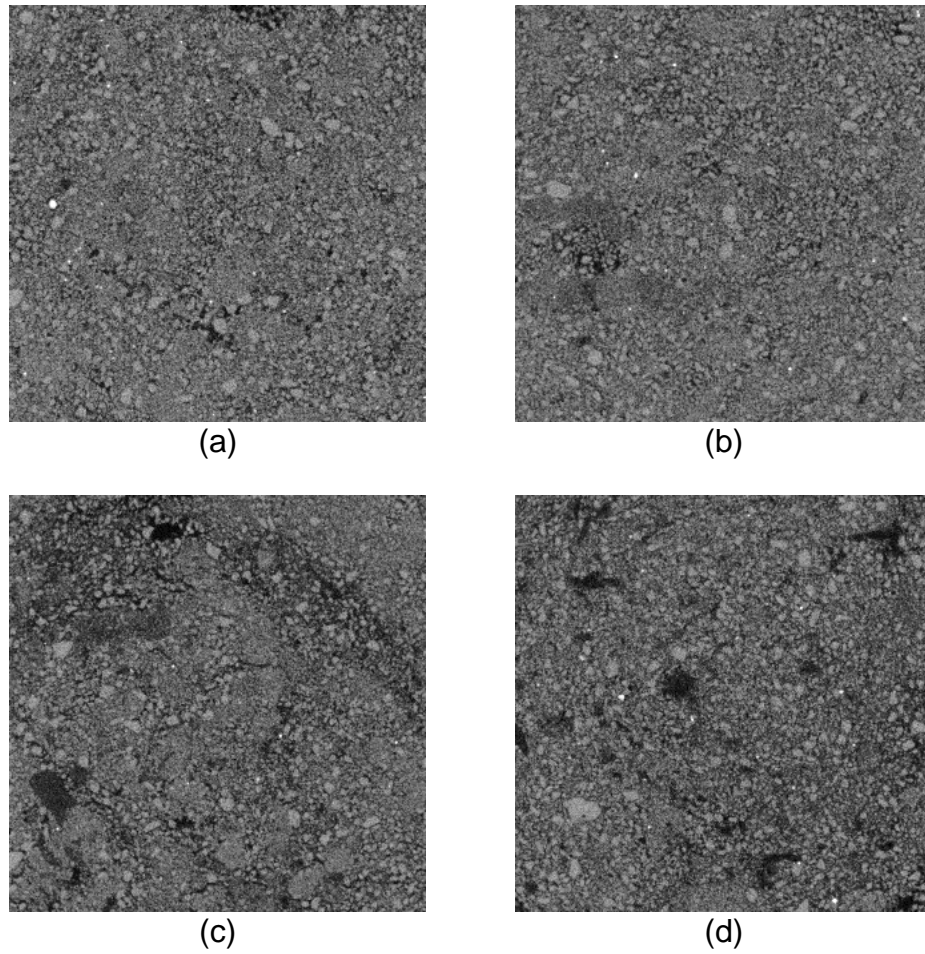


Figure 1. Four examples of 2D images (790x790 pixels) from a sugar cane plantation soil sample: (a) slice_001, (b) slice_100, (c) slice_395 and (d) slice_790.

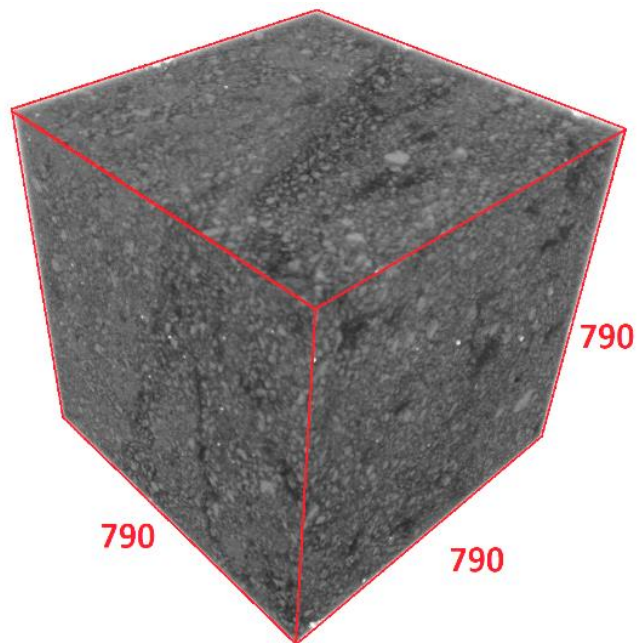


Figure 2. 3D representation of a sugar cane plantation soil sample.

Despite advances in the resolution of CT equipment and computer power, there is no consensus on data analysis methods that can reveal the complexity of all elements associated with 3D soil images, especially methods that do not require a threshold to segment images. In this context, this work employs two methods originally developed for the analysis of complex signals, Detrended Fluctuation Analysis (DFA) and Fisher-Shannon (FS), to bring new understanding of the complexity of morphological properties of soil based on the analysis of 3D CT images. Up to date these two methods have not been used in 3D image analysis.

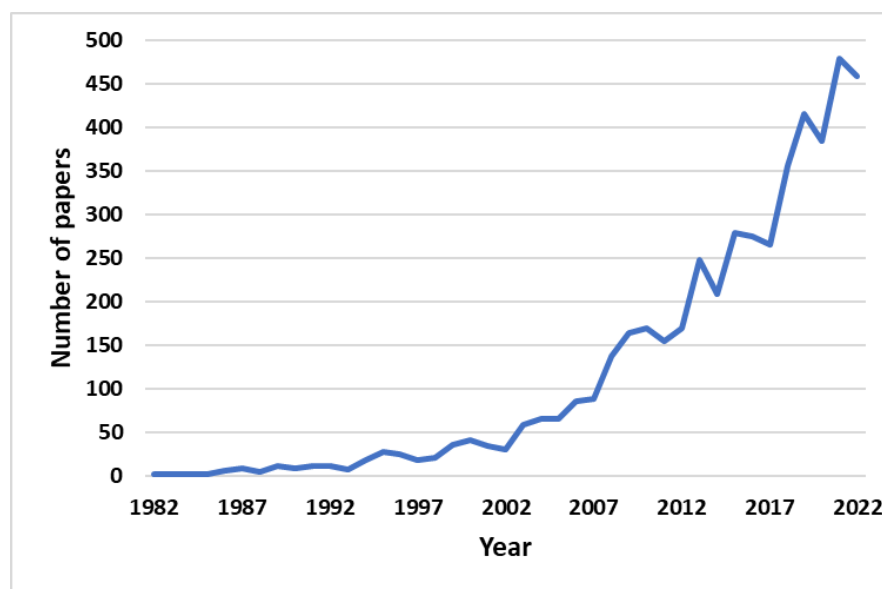


Figure 3. Publications using the terms "tomography" and "soil" from 1982 to 2022, according to the Scopus database.

The DFA method is a tool typically used to analyze time series data to detect the presence of long-range correlations in non-stationary series. The advantage of DFA is that it can systematically eliminate trends of different orders (KANTELHARDT *et al.*, 2001). The DFA method was initially proposed by Peng *et al.* (PENG *et al.*, 1994) in 1994 to analyze the organization of nucleotides in a DNA chain. Currently, several recent applications of DFA can be found in various areas of knowledge, such as physiology (BLOKHINA *et al.*, 2023; VAZ; SILVA; STERGIU, 2023), climatology (KIRÁLY; JÁNOSI, 2005; MALLICK *et al.*, 2021; TATLI; DALFES, 2020), economics (KRISTOUFEK, 2019; MOHTI *et al.*, 2019), engineering (BOUNOUA; AFTAB; OMLIN, 2023; LIU; CHEN; ZHANG, 2020), sport (FERREIRA, 2018), and seismology (KATAOKA; MIYAGUCHI; AKIMOTO, 2021; SKORDAS; CHRISTOPOULOS;

SARLIS, 2020), among others. However, applications of DFA involving soil data are rare, among them three can be cited: the first that identifies active erosion sites (CAO *et al.*, 2020); another that analyzes patterns of water storage in soil (BISWAS; ZELEKE; SI, 2012); and the third that analyzes time series of radioactive elements in soil (RAFIQUE *et al.*, 2021). However, all three applications employ the multifractal version of DFA – Multifractal Detrended Fluctuation analysis (MFDFA), to analyze time series (RAFIQUE *et al.*, 2021) or one - dimensional spatial data (BISWAS; ZELEKE; SI, 2012; CAO *et al.*, 2020). In this work 3D soil tomographic images were analyzed using DFA in its original form and its generalization for 2D and 3D data (AGUIAR *et al.*, 2022).

The FS method is a statistical technique originated in information theory that consists of a joint analysis of Fisher's information measure (FIM) (FISHER, 1925), which quantifies the amount of organization (or order) in a signal, and Shannon entropy (SE) (SHANNON, 1948), which quantifies the degree of uncertainty (or disorder) (LOVALLO; PIERINI; TELESKA, 2012). Recent applications of the Fisher-Shannon method can be found in various areas of science, such as ecology (BA *et al.*, 2020; TELESKA *et al.*, 2022), economics (FERNANDES; DE ARAUJO; SILVA, 2022; KWAPIÉ *et al.*, 2023), physics (DEHESA, 2023; MARTÍNEZ-FLORES, 2021), physiology (FUENTES *et al.*, 2022) and climatology (DA SILVA *et al.*, 2021) among others. However, applications of the Fisher-Shannon method in soil data are scarce. One of these few applications relates seismic microtremors to soil type through FS analysis (TELESKA *et al.*, 2015) analysis but does not use soil tomographic images in the analysis. Another application is a partial result of this work, which quantifies the complexity of soil using FS of 3D tomographic images. In this work (STOSIC *et al.*, 2022) the complexity of soil 3D tomographic images was analyzed through the application of FS method on the probability distribution of gray scale values of one dimensional columns extracted from 3D images.

Both methods DFA and FS were used to analyze 24 3D tomographic images extracted from soil samples from the Northeast region of Brazil, specifically in the state of Pernambuco between latitudes -7.84836 and -7.83519, and longitudes -34.9973 and -34.9935. Out of these images, 12 are from soil samples from the Atlantic Forest, and 12 are from sites where native vegetation of Atlantic Forest was replaced by sugarcane plantations.

The main objective of this work is to investigate complexity of morphological properties of soil under different land use. More specifically, it aims to:

- Apply the DFA method for 1, 2 and 3 dimensional data to 3D soil images to quantify long-range correlations (persistence of density fluctuation);
- To compare the performance of 1D, 2D, and 3D DFA methods to distinguish between soil properties under different land cover (Atlantic Forest and sugarcane plantations);
- Verify if the information quantifiers of 3D soil images obtained by the Fisher-Shannon method capture changes in land use;
- Quantify the complexity of soil samples in terms of distance from the isocomplexity line in the FS plane;
- Propose a new procedure for normalization of FS quantifiers for representation on the Fisher-Shannon information plane while preserving the Fisher Shannon complexity.

2. Detrended fluctuation analysis of three-dimensional data: application to soil X-ray CT scans

2.1 Abstract

In this work we compare three distinct schemes for Detrended Fluctuation (DFA) analysis of 3D $N \times N \times N$ data sets: i) a $N \times N$ set of 1D DFA runs for each vertical line of length N , ii) a set of N 2D DFA runs for each of the $N \times N$ planes along the z direction, and iii) a single 3D DFA run. The objective of this work is twofold: i) to compare the performance of 1D, 2D and 3D DFA methods in terms of compatibility as well as the richness of obtained results, and ii) to demonstrate how these three complementary approaches shed new light on the complexity of the structure of the two real soil samples, through the analysis of grayscale high-resolution X-ray CT scan images.

Keywords: Detrended fluctuation analysis; three-dimensional data; X-ray CT scan soil samples.

2.2 Introduction

Analysis of three-dimensional data sets (images) has been gaining momentum over the years in diverse scientific and technological fields, with the advance of both technological data acquisition methods, and high-performance computational resources. A three-dimensional image may be composed in different ways, e.g. by merging satellite images acquired at successive time frames for a composite spatiotemporal analysis, but probably the most widespread applications stem from computed tomography (CT) scans.

The dramatic increase in the performance of CT scanners in terms of resolution and image quality has led to their widespread use principally in medicine, but applications in other fields of science and technology have also been experiencing a dramatic rise. On the other hand, the analysis of high-resolution images may pose computational challenges, as e.g., a $1000 \times 1000 \times 1000$ resolution image is composed

of one billion voxels (volume elements), represented by their gray scale values, that may turn out too demanding for many standard tools.

In this work, we explore the application of detrended fluctuation analysis (DFA) on 3D images to quantify long-range correlations at different scales, with an example of high-resolution soil CT scan images. The DFA method was introduced in 1994 by Peng et al (PENG *et al.*, 1994) to study correlations in non-stationary time series, and has been subsequently applied in diverse fields of science. More recently, a generalization of the DFA method was proposed by Gu and Zhou (GU; ZHOU, 2006), followed by only several applications up to date for 2D data sets, and to the best of our knowledge no applications have been published yet for 3D data. We consider here (and compare the results of) three distinct schemes for DFA analysis of $N \times N \times N$ 3D soil samples: i) a $N \times N$ set of 1D DFA runs for each vertical line, ii) a set of N 2D DFA runs for each of the $N \times N$ planes along the vertical direction, and iii) a single 3D DFA run. The results of all three approaches are shown to be compatible.

The choice of soil CT scan images for the examples studied here stems from the fact that a deeper understanding of the physical, chemical and biological processes within soil depends on the quantification of heterogeneity and complexity of the spatial distribution of soil particles and aggregates (SCHLÜTER *et al.*, 2018). X-ray CT scans have already been employed for quantification of the physical structure and spatial distribution of the pore space (HOUSTON *et al.*, 2017), revealing extraordinary complexity of this system (FALCONER *et al.*, 2012; JUAREZ *et al.*, 2013; KATUWAL *et al.*, 2015). The complexity of soil structure has also been assessed by using methods based on concepts from statistical physics such as fractals and multifractals (LUO; LIN, 2009; PERRET; PRASHER; KACIMOV, 2003; SAN JOSÉ MARTÍNEZ *et al.*, 2010; WANG *et al.*, 2016), information content (TORRE *et al.*, 2020) and complex networks (CÁRDENAS *et al.*, 2010; SAMEC *et al.*, 2013). As there remains a lack of consensus on the appropriate poresolid CT threshold (GIBSON; LIN; BRUNS, 2006; TARQUIS *et al.*, 2009; TORRE *et al.*, 2020), it has also been suggested that grayscale soil images should be used for multifractal characterization of the soil structure, rather than thresholding (ROY; PERFECT, 2014; TORRE *et al.*, 2018; TORRE; LOSADA; TARQUIS, 2018; ZHOU *et al.*, 2010, 2011).

In this work, we analyze two 790x790x790 greyscale level X-ray CT scan images of real soil samples, from a sugar cane field, and a nearby Atlantic Forest site, in northeastern Brazil. The objective of this work is twofold: i) to compare the

performance of 1D, 2D and 3D DFA methods, and ii) to demonstrate how this approach sheds new light on the complexity of the structure of the two real soil samples. In the next section we describe the methodology, then we show the results with discussion, and finally we draw the conclusions.

2.3 Methodology

2.3.1 Detrended fluctuation analysis (1D DFA)

Detrended fluctuation analysis (DFA) was introduced by Peng et al. (PENG *et al.*, 1994) as a method for quantification of correlations in non-stationary time series (CHEN *et al.*, 2002; HU *et al.*, 2001; KANTELHARDT *et al.*, 2001). This method represents a modified root-mean-square analysis of a random walk, and has been subsequently successfully applied in a wide spectrum of areas, ranging from physiology (GOLDBERGER *et al.*, 2002; LI *et al.*, 2019), to geophysics (CURRENTI *et al.*, 2005), climatology (KIRÁLY; JÁNOSI, 2005; STOSIC; TELESCA; STOSIC, 2021), and finances (DE LIMA *et al.*, 2018; YAMASAKI *et al.*, 2005), to name just a few.

For a random sequence of (positive and negative) increments (random walk steps), the implementation of the DFA algorithm is described as follows:

- i) The original series $x(i), i = 1, \dots, N$ is integrated to yield

$$X(k) = \sum_{i=1}^k [x(i) - \langle x \rangle] \quad , \quad k = 1, 2, \dots, N$$

where $\langle x \rangle = \sum_{i=1}^N x(i)/N$ is the average. This step is necessary to transform the original series of random walk steps into a “profile” (series of the random walk displacements), and should be omitted if the actual data represent a profile, rather than steps.

- ii) Next, the integrated series $X(k)$ is divided into $N_n = [N/n]$ non-overlapping segments of length n (here $[\cdot]$ stands for the integer value of the argument), and in each segment $s = 1, \dots, N_n$ the local trend $X_{n,s}(k)$ (linear or higher-order

polynomial least squares fit – termed DFA1, DFA2, DFA3,..., for polynomials of order 1,2, 3,..., respectively) is estimated and subtracted from $X(k)$. In DFA m , trends of order m in the profile $X(k)$, and of order $m - 1$ in the original record $x(i)$ are eliminated.

iii) The detrended variance is now calculated as

$$F^2(n) = \frac{1}{nN_n} \sum_{s=1}^{N_n} \sum_{k=(s-1)n+1}^{sn} [X(k) - X_{n,s}(k)]^2.$$

iv) Repeating this calculation for different segment sizes provides the relationship between the fluctuation function $F(n)$ and the segment size n . If long-term correlations are present in the original series, $F(n)$ increases with n according to a power law

$$F(n) \sim n^{\alpha_1}.$$

The scaling exponent α is obtained as the slope of the linear regression of $\log F(n)$ versus $\log n$. The value $\alpha_1 = 0.5$ indicates the absence of correlations (white noise), $\alpha_1 > 0.5$ indicates the persistence of long-term correlations, meaning that large (small) values are more likely to be followed by large (small) values, while $\alpha_1 < 0.5$ indicates antipersistent long-term correlations, meaning that large values are more likely to be followed by small values, and vice versa. The values $\alpha_1 = 1$ and $\alpha_1 = 1.5$ correspond to $1/f$ noise and Brownian noise (integration of white noise), respectively (PENG *et al.*, 1994), and values of $\alpha_1 > 1.0$ are obtained for fractional Brownian motion (when a series of displacements is integrated).

2.3.2 Detrended fluctuation analysis in two dimensions (2D DFA)

More recently, Guo and Zheng (GU; ZHOU, 2006) have generalized the above described one-dimensional DFA algorithm for higher dimensions. Up to date, there have been several implementations of this method (ALPATOV; VIKHROV; GRISHANKINA, 2013; ALVAREZ-RAMIREZ *et al.*, 2008; BARRERA *et al.*, 2010; LIU *et al.*, 2017; NIE *et al.*, 2015; VARGAS-OLMOS *et al.*, 2015; VELAZQUEZ-CAMILO *et al.*, 2010) in two-dimensions, for which the approach consists of the following steps.

- i) A self-similar surface represented by two-dimensional $N \times M$ matrix $x(i, j)$, $i = 1, \dots, N$ and $j = 1, \dots, M$ is divided into $N_n \times M_n$ square non-overlapping segments of size $n \times n$, where $N_n = [N/n]$ and $M_n = [M/n]$.
- ii) In each segment indexed by $s = 1, \dots, N_n$ and $t = 1, \dots, M_n$, consisting of data points $x(i, j)$ with $i = (s - 1)n + 1, \dots, sn$, $j = (t - 1)n + 1, \dots, tn$, data are integrated to produce the profile

$$X_{s,t}(k, l) = \sum_{i=1}^k \sum_{j=1}^l x((s - 1)n + i, (t - 1)n + j), \quad k, l = 1, \dots, n$$

Note that the order of these two first steps has been reversed in comparison with the 1D DFA approach, but this is relevant only for multifractal generalization (GU; ZHOU, 2006), which is not being addressed here. Again, this step should be omitted if the actual data correspond to a profile rather than local fluctuations, in which case the profile segment simply consists of the data points $X_{s,t}(k, l) = x((s - 1)n + k, (t - 1)n + l)$, for $k, l = 1, \dots, n$.

- iii) Next, the local trend $\tilde{X}_{s,t}(k, l)$ is captured for each segment by least-squares fitting to a linear (or higher-order polynomial) bivariate function, and subtracted from $X_{s,t}(k, l)$ to find the residuals, from which the detrended variance is calculated for each segment as

$$F^2(s, t, n) = \frac{1}{n^2} \sum_{k=1}^n \sum_{l=1}^n \left(X_{s,t}(k, l) - \tilde{X}_{s,t}(k, l) \right)^2$$

It was shown in (GU; ZHOU, 2006) that linear interpolation of the form $a + bk + cl$ works rather well.

- iv) Finally, the fluctuation function $F(n)$ at scale n is now calculated as

$$F(n) = \left\{ \frac{1}{N_n M_n} \sum_{s=1}^{N_n} \sum_{t=1}^{M_n} F^2(s, t, n) \right\}^{1/2} .$$

- v) As before, repeating this calculation for different segment sizes provides the relationship between the fluctuation function $F(n)$ and the segment size n . If long-range correlations are present in the original data set, $F(n)$ increases with n according to a power law

$$F(n) \sim n^{\alpha_2}$$

where the (2D DFA) scaling exponent α_2 is obtained as the slope of the linear regression of $\log F(n)$ versus $\log n$. It describes the long-range power-law correlation properties of the surface and can be seen as a measure of surface texture (or roughness). The value $\alpha_2 = 0.5$ corresponds to non-correlated surfaces, while $\alpha_2 > 0.5$ and $\alpha_2 < 0.5$ correspond to persistent and antipersistent correlations of the surface fluctuations (GU; ZHOU, 2006).

2.3.3 Detrended fluctuation analysis in three dimensions (3D DFA)

While the Guo and Zheng (GU; ZHOU, 2006) generalization in principle covers any dimension above unity, they mention that they have tested the approach on synthetic datasets, but they do not provide explicit formulas. Moreover, to the best of our knowledge no works have been published up to date for DFA analysis of three-dimensional (or higher dimensional) data. It may be inferred from (GU; ZHOU, 2006) that for 3D, the approach consists of the following steps.

- i) A self-similar volume represented by a three-dimensional $N \times M \times P$ matrix $x(i, j, k)$, $i = 1, \dots, N$, $j = 1, \dots, M$ and $k = 1, \dots, P$ is divided into $N_n \times M_n \times P_n$ cubic non overlapping segments (boxes) of size $n \times n \times n$, where $N_n = [N/n]$, $M_n = [M/n]$ and $P_n = [P/n]$.
- ii) In each box segment indexed by $r = 1, \dots, N_n$, $s = 1, \dots, M_n$ and $t = 1, \dots, P_n$, consisting of data points $x(i, j, h)$ with indices $i = (r - 1)n + 1, \dots, rn$, $j = (s - 1)n + 1, \dots, sn$, and $h = (t - 1)n + 1, \dots, tn$, data are integrated to produce the profile

$$X_{r,s,t}(k, l, m) = \sum_{i=1}^k \sum_{j=1}^l \sum_{h=1}^m x((r - 1)n + i, (s - 1)n + j, (t - 1)n + h), \quad k, l, m = 1, \dots, n$$

Again, this step should be omitted if the actual data correspond to a profile, rather than local fluctuations, in which case the profile segment simply consists of the data points $X_{r,s,t}(k, l, m) = x((r - 1)n + k, (s - 1)n + l, (t - 1)n + m)$, for $k, l, m = 1, \dots, n$.

- iii) Next, the local trend $\tilde{X}_{r,s,t}(k, l, m)$ is captured for each segment by least-squares fitting to a linear (or higher-order polynomial) function of three variables, and subtracted from $X_{r,s,t}(k, l, m)$ to find the residuals, from which the detrended variance is calculated for each segment as

$$F^2(r, s, t, n) = \frac{1}{n^3} \sum_{k=1}^n \sum_{l=1}^n \sum_{m=1}^n \left(X_{r,s,t}(k, l, m) - \tilde{X}_{r,s,t}(k, l, m) \right)^2$$

In what follows, we shall apply linear interpolation of the form $a + bk + cl + dm$.

- iv) Finally, the fluctuation function $F(n)$ at scale n is now calculated as

$$F(n) = \left\{ \frac{1}{N_n M_n P_n} \sum_{r=1}^{N_n} \sum_{s=1}^{M_n} \sum_{t=1}^{P_n} F^2(r, s, t, n) \right\}^{1/2} .$$

- v) Repeating this calculation for different segment sizes again provides the relationship between the fluctuation function $F(n)$ and the segment size n . If long-range correlations are present in the original data set, $F(n)$ increases with n according to a power law

$$F(n) \sim n^{\alpha_3}$$

where the (3D DFA) scaling exponent α_3 is obtained as the slope of the linear regression of $\log F(n)$ versus $\log n$. It describes the long-range power-law correlation properties of the surface and can be seen as of a measure of surface texture (or roughness). The value $\alpha_3 = 0.5$ corresponds to non-correlated volume, while $\alpha_3 > 0.5$ and $\alpha_3 < 0.5$ correspond to persistent and antipersistent correlations of the volume fluctuations.

2.3.4 Soil samples

Soil samples were collected from a field cultivated with sugarcane and from a nearby native Atlantic Forest site, located in the state of Pernambuco, northeastern Brazilian region. The samples were obtained using a soil auger with an internal PVC cylinder of 7.5 cm height by 7.5 cm diameter, excavated by careful penetration with a cylinder coupled with a blade. After the insertion of the auger in the soil, the cylinders were carefully extracted to ensure the preservation of the original structure of the environment inside the PVC cylinders. The samples were then dried at 40°C to remove the water content, before the scanning tomography of the samples. The CT tomography was performed using a third-generation Nikon XT H 225 ST X-ray microtomography equipment with 150 kV voltage, 180 μ A current, 500 ms exposure time, and a 45 μ m resolution for voxels. A copper filter with a thickness of 0.5 mm was used to minimize low-intensity photons. After the scanning of the total cylinder volume in the preliminary acquisition, a subvolume of interest was defined and reconstructed using CTPro 3D XT 3.0.3 (Nikon Metrology NV) software. The central part of the cylinder was highlighted to avoid edge influence. The reconstructed 2D axial projections maintained the same spatial resolution of the acquisition of 45 μ m, and were saved at a radiometric resolution (gray scale level) of 16 bits. The final volume was 790 stacks with 790 x 790 pixels, with an end volume of $790^3 = 493,039,000$ voxels.

The voxel values of the CT scan images correspond to local sample density, and the sequence of values in any direction is interpreted here as the integrated series, that is, a profile with random (but correlated) increments. Therefore, in what follows, the integration step is omitted in all three versions of the DFA method. Moreover, the vertical (gravity) direction may be here considered as naturally preferential from a phenomenological point of view, but we have performed calculations in all three directions, and have found no significant anisotropy difference. Therefore, henceforth only the results in the vertical direction are reported.

2.4 Results and discussion

The 1D DFA method was applied here for $790 \times 790 = 624,100$ vertical soil sample lines of length 790, across the sample area, emulating a time series of observations of

a virtual observer, descending down the sample at constant speed, at all the different points of the cross-sectional area. The descriptive statistics, the histograms, and spatial distribution of the 1D DFA exponents for the two samples, are presented in table 1, figure 1 and figure 2, respectively. The 1D DFA exponent distributions are found to be statistically the same in all three directions (no anisotropy was observed).

Table 1. Descriptive statistics of DFA exponent values for the two samples.

	Minimum	1°Quartile	Median	Mean	3°Quartile	Maximum	Standard Deviation
Sugarcane	0.1141	0.2085	0.2255	0.2272	0.2440	0.4725	0.0272
Atlantic Forest	0.1534	0.2703	0.2907	0.2917	0.3119	0.5129	0.0311

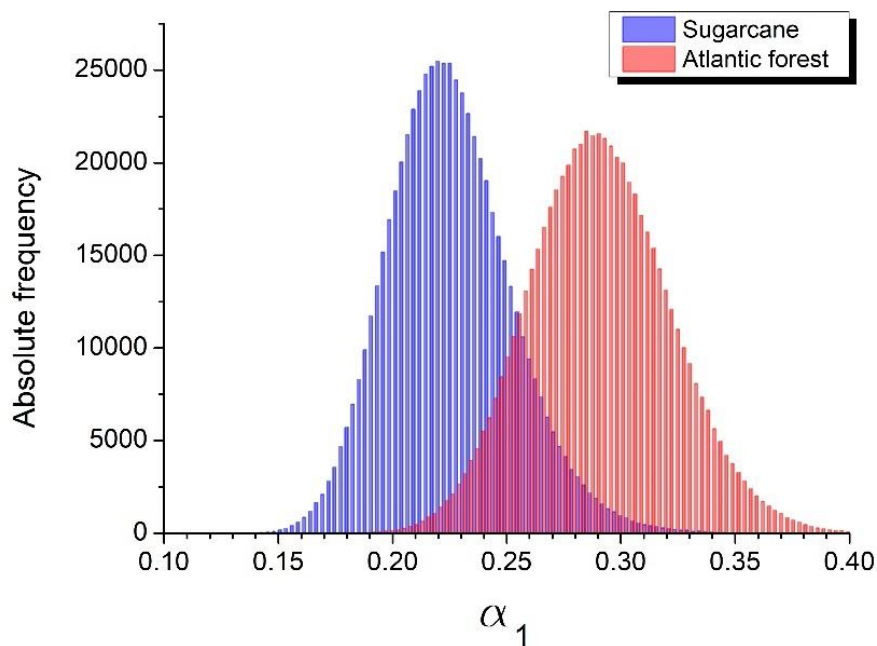


Figure 1. 1D DFA exponent value histograms for the two samples.

It is seen from table 1 and figure 1 that fluctuations of soil density along the vertical direction are strongly antipersistent, with somewhat stronger pronounced antipersistence for the sugar cane sample, in comparison with the Atlantic Forest sample. The intricate spatial distribution of 1D DFA exponents displayed in figure 2 suggests that the local sugarcane soil fluctuations are somewhat more homogeneous than those of the Atlantic Forest.

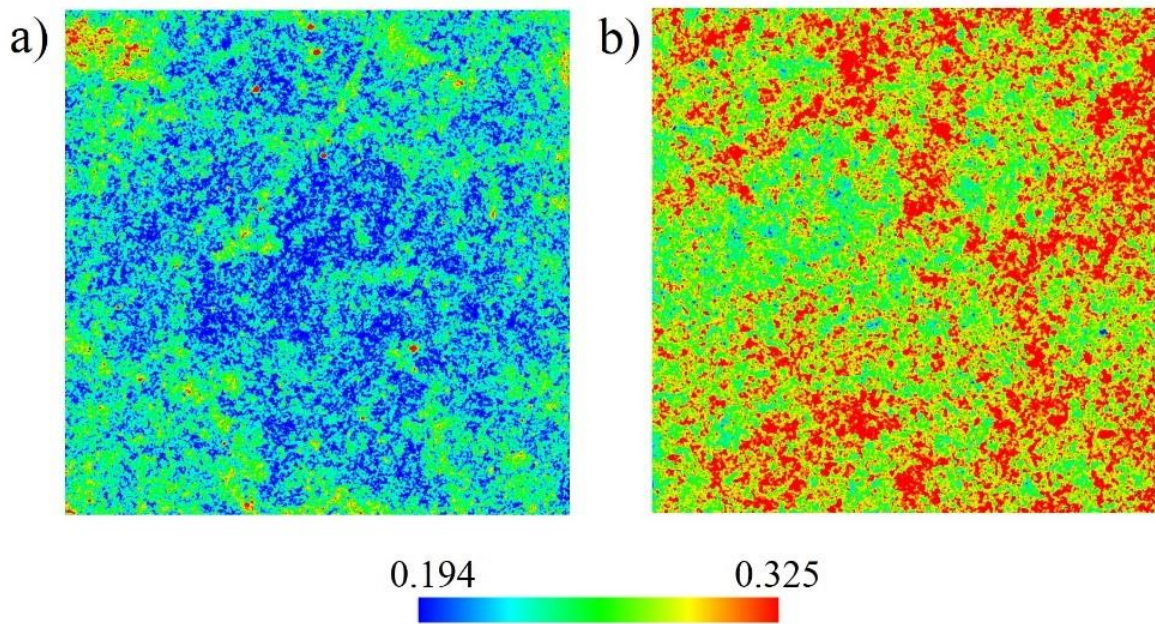


Figure 2. Color coded DFA exponent values for a) sugarcane, and b) Atlantic Forest sample. The color coding scheme was chosen to emphasize the contrast among the samples, with bounds corresponding to ± 1.5 standard deviations of the composite sample, from the composite mean.

The 2D DFA method was then implemented for 790 vertical soil sample cross-sections, of 790x790 voxels each. The descriptive statistics, the histograms, and vertical spatial distribution of the 2D DFA exponents for the two samples, are presented in table 2, figure 3, and figure 4, respectively.

Table 2. Descriptive statistics of 2D DFA exponent values for the two samples.

	Minimum	1 ^o Quartile	Median	Mean	3 ^o Quartile	Maximum	Standard Deviation
Sugar cane	0.1625	0.1835	0.1911	0.1912	0.1978	0.2224	0.0119
Atlantic Forest	0.2538	0.2618	0.2672	0.2699	0.2750	0.3076	0.0113

By comparing the results of the 1D DFA presented in table 1 and the 2D DFA presented in table 2, we can confirm that overall the two approaches are compatible: they both show stronger antipersistence of local density fluctuations for the sugar cane sample, in comparison with that of the Atlantic Forest sample, although for both samples the 1D DFA yields somewhat higher exponent values (less pronounced antipersistence), in comparison with the 2D DFA. Moreover, the 1D DFA explores the

vertical antipersistence of density fluctuations across the sample cross-section, revealing the intricate structure of this feature for the chosen projection.

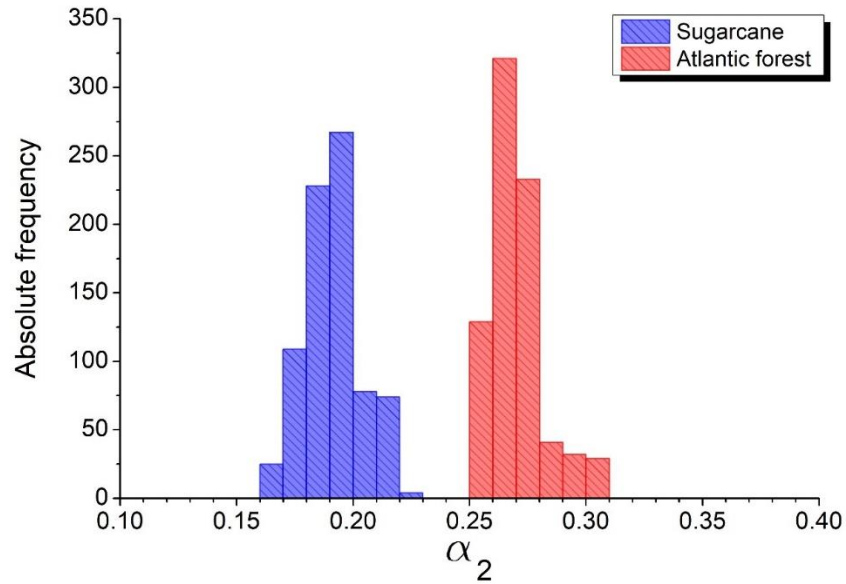


Figure 3. 2D DFA exponent value histograms for the two samples.

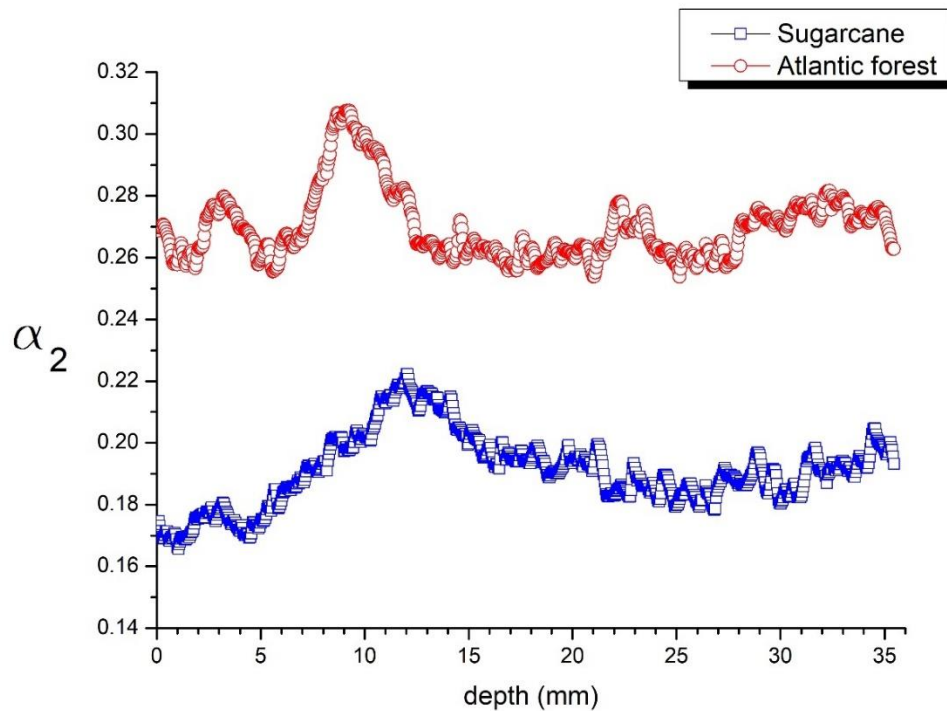


Figure 4. 2D DFA exponent values for the two samples, as a function of depth.

Finally, the 3D DFA method yields only two exponent values of $a_3 = 0.2005$ for the sugarcane sample, and $a_3 = 0.2696$ for the Atlantic Forest, rather close to the means of the 2D DFA exponents given in table 2. Comparing all three methods, we can state here that all three yield rather similar results: all three methods indicate strong antipersistence of local density fluctuations, which are consistently stronger (lower exponent value) for the sugar cane sample, than for the Atlantic Forest.

In terms of computational effort and memory requirements, there is no significant difference among the three methods described here (all calculations were performed on an Intel I7-6700HQ processor, in an order of several hours). All three methods also arrive at rather similar quantitative measures of local fluctuation antipersistences, confirming the consistency of the current approach. On the other hand, the multiple 1D approach does seem to provide the most insight into the phenomenon (e.g. the homogeneity and/or the spatial distribution of the 1D DFA exponents observed in figure 2), while sacrificing the separation of the two samples, observed in Figs 1 and 3.

2.5 Conclusions

In terms of comparison of the three schemes of application of the DFA method for three dimensional datasets, we may conclude that the three considered approaches: i) an $N \times N$ set of 1D DFA runs for each vertical line of length N , ii) a set of N 2D DFA runs for each of the $N \times N$ planes along the vertical direction, and iii) a single 3D DFA run, all yield rather compatible results. More precisely, the 1D DFA yields somewhat higher DFA exponent values (indicate somewhat lower antipersistence) than those of the 2D and 3D DFA (which are practically the same), but the ranking of the results is preserved: sugar cane sample demonstrates lower exponent values (stronger antipersistence) than the Atlantic Forest sample, in all three cases. The fact that the 1D DFA exponent is somewhat higher may be seen as somewhat surprising, as one could well assume *a priori* that whatever antipersistence is observed in a one-dimensional sample would be “weakened” when the analysis is extended to two or three dimensions. This could be explained by finite size scaling effects (the sheer sample size): in 1D DFA we are dealing with 624,100 samples of length 790, in 2D DFA there are 790 samples of size $790^2=624,100$, and for the 3D DFA there is a single

sample of size $790^3=493,039,000$. Apparently, the 2D and the 3D samples are large enough to capture the full level of the relation among local density fluctuations, while the 1D DFA does not capture the full level of antipersistence, but it provides a more intricate description of the spatial distribution of antipersistence of local density fluctuation. As all three approaches are similar in terms of necessary computational effort, we may conclude that all three should be used in unison, complementing the phenomenological picture.

Comparing the current study with previous works that have addressed fractal and multifractal properties of high resolution 2D and 3D CT scan soil samples (LUO; LIN, 2009; PERRET; PRASHER; KACIMOV, 2003; ROY; PERFECT, 2014; SAN JOSÉ MARTÍNEZ *et al.*, 2010; TORRE *et al.*, 2018; TORRE; LOSADA; TARQUIS, 2018; WANG *et al.*, 2016; ZHOU *et al.*, 2010, 2011), it should be emphasized here that all these works deal with the spatial arrangement of voxels. In (LUO; LIN, 2009; PERRET; PRASHER; KACIMOV, 2003; SAN JOSÉ MARTÍNEZ *et al.*, 2010; WANG *et al.*, 2016) thresholding is used to extract the information on pores, and then boxcounting is implemented to study fractal (LUO; LIN, 2009; PERRET; PRASHER; KACIMOV, 2003) and multifractal (SAN JOSÉ MARTÍNEZ *et al.*, 2010; WANG *et al.*, 2016) behavior. In (ZHOU *et al.*, 2010, 2011), Zhou et al. analyze 2D high resolution grayscale soil sample images, wherefrom partition function is constructed to examine multifractal behavior. In a follow-up of this work, Roy and Perfect (ROY; PERFECT, 2014) study 2D grayscale images in terms of lacunarity and multifractal behavior. Finally, Torre et al (TORRE *et al.*, 2018; TORRE; LOSADA; TARQUIS, 2018) implement cube gliding on CT grayscale soil images to construct the partition function and therefrom derive the multifractal spectrum.

In the current work we adopt a rather different approach: we deal with local density fluctuations, that is, the density difference among neighboring sites (voxels). More precisely, consider a (tiny) observer that can freely hop from site (voxel) to site (another voxel), in one, two, or three dimensions. At each hop, the observer registers a change of density of the environment (voxel, at current experimental resolution). The question is: are these changes random? It turns out that they are not, instead, they are “antipersistent”: small changes are more likely to be followed by large changes along the way (in one, two or three dimensions), and vice versa. Moreover, this antipersistence effect is more pronounced in the sugarcane soil sample than in the

Atlantic Forest sample. Whatever may be the practical implications of these phenomenological findings remains to be seen, but as such, we believe that the current work provides a complementary contribution to the understanding of this extremely complex phenomenon: the spatial arrangement of constituent soil particles.

Finally, it should be stressed here that the current approach of combining 1D, 2D and 3D DFA analysis for three-dimensional images is quite general, and can be applied in studies of diverse phenomena.

3. Quantifying soil complexity using Fisher-Shannon method on 3D X-ray CT scans

3.1 Abstract

The conversion of native forests into agricultural land, common in many parts of the world, poses important questions regarding soil degradation, demanding further efforts to understand better the effect of land use change on soil functions. With the advent of 3D Computed Tomography techniques and computing power, new methods are becoming available to address this question. In this direction, in the current work, we modify the Fisher-Shannon method, borrowed from information theory, to quantify the complexity of 12 3D CT soil samples from a sugarcane plantation and 12 samples from a nearby native Atlantic Forest northeastern Brazil. The distinction between the samples from the sugar plantation and the Atlantic Forest site is quite pronounced. The results at 91.7% accuracy were obtained considering the complexity of the Fisher-Shannon plane. Atlantic Forest samples are generally more complex than those from the sugar plantation.

Keywords: complexity, Fisher Shannon plane, land use change, X-ray CT scan soil samples.

3.2 Introduction

The degradation of soils due to land use changes driven by economic factors represents a major concern in many parts of the world for the foreseeable future. Land use change may adversely affect fundamental soil functions such as nutrient storage, diffusion and cycling, carbon storage and greenhouse gas emissions, erosion resistance, water storage, drainage, and filtration (BREUER; PAPEN; BUTTERBACH-BAHL, 2000; LABRIÈRE *et al.*, 2015; TELLES *et al.*, 2003; WILCKE *et al.*, 2002; WOHL *et al.*, 2012). Moreover, the biodiversity of forests may also be unfavourably affected by systematic land use change (FUJII *et al.*, 2018). On the other hand, poverty and population growth lead to an ever-increasing demand for indiscriminate natural

resources in developing countries. The demand for pasture, timber, firewood, and crops drives the conversion of tropical forests into agricultural land at an alarming rate. This situation dictates comprehensive studies on the impact of deforestation and land use conversion on soil quality in general. More precisely, the outstanding question is whether the cultivation of deforested land may lead to the permanent degradation of land productivity. The ecologically sensitive components of the tropical ecosystem may not buffer the effects of agricultural practices, see, e.g. (ISLAM; WEIL, 2000) and references therein. Therefore, a comprehensive assessment of soil properties is fundamental for the early detection and mitigation of adverse soil change effects.

The effects of land use change have been addressed mainly focusing on physical, chemical, and biological properties (ISLAM; WEIL, 2000; LEMENIH; KARLTUN; OLSSON, 2005; MAHARJAN *et al.*, 2017), while far fewer studies have been devoted to changes in soil structure (WANG *et al.*, 2019; ZHOU *et al.*, 2012). The latter governs its functions (RABOT *et al.*, 2018), and quantification of soil architecture can be seen as a key to better understanding the complex dynamical phenomena that govern these functions. Therefore, a comprehensive description and quantification of soil functions rely on an in-depth understanding of the characteristics such as the three-dimensional distribution of constituents, connectedness, hierarchical organization, and complexity.

While X-ray computed tomography (CT) has been advancing at an impressive rate over the last decades, it has also become a widespread tool for non-destructive 3D soil visualization and quantification, shedding new light on soil functions (HELLIWELL *et al.*, 2013). Diverse properties of soil that have not been previously amenable to analyses can now be assessed through CT scans, providing novel fundamental insights into soil functions (HELLIWELL *et al.*, 2013). These properties include isotropy, homogeneity, complexity, and hierarchical fractal (or multifractal) organization of soil constituents. They contribute to a deeper understanding of soil's physical, chemical, and biological processes (SCHLÜTER *et al.*, 2018). X-ray CT scans have already been studied to characterize the pores spatial distribution, revealing the extraordinary complexity of the pore space (GALDOS *et al.*, 2019; JUAREZ *et al.*, 2013; PIRES *et al.*, 2019; SANTOS *et al.*, 2020). The complexity of soil structure has also been addressed through methods based on concepts from statistical physics and information theory, such as fractals and multifractals (PERRET; PRASHER; KACIMOV, 2003; SAN JOSÉ MARTÍNEZ *et al.*, 2010; WANG *et al.*, 2016),

information content (TORRE *et al.*, 2020) and complex networks (CÁRDENAS *et al.*, 2010; SAMEC *et al.*, 2013). As a consensus has not yet been reached on the adequate threshold for separating pores from solids in CT scans (TARQUIS *et al.*, 2009), it has also been suggested that rather than thresholding, grayscale soil images should be used for multifractal characterization of the soil structure (ROY; PERFECT, 2014; TORRE *et al.*, 2018; TORRE; LOSADA; TARQUIS, 2018; ZHOU *et al.*, 2010, 2011).

Between 2000 and 2018, Brazil suffered a total reduction of 489,877 km² in the natural area of its six terrestrial biomes. Among them, the Atlantic Forest biome is the one with the highest percentage of degradation over time, as it covers the most industrialized and productive areas, in addition to having the highest demographic density in the national territory, housing about 49.3% of the urban areas of the country (IBGE, 2020). One of the crops that stands out in the Atlantic Forest biome is sugarcane, especially in the country's northeast region, where cultivation is present in eight of the nine states in the region. For the 2020/2021 harvest, an increase of 1.6% in the planted area and 4.1% in production were estimated compared to the previous sugarcane harvest in the northeastern region of Brazil (CONAB, 2020). The replacement of the native vegetation of the Atlantic Forest with sugarcane cultivation generates negative impacts on the physical attributes of the soil (BORDONAL *et al.*, 2018; CASTIONI *et al.*, 2018; CAVALCANTI *et al.*, 2020; ORTIZ *et al.*, 2017). These attributes control many soil functions, such as water retention and infiltration, gas exchange, resistance to erosion, nutrient dynamics, and root penetration (RABOT *et al.*, 2018), and directly influence ecosystem services.

In this work, we investigate how land use change affects soil structure using information theory to quantify the complexity of soil 3D X-ray CT soil samples. For the first time, the Fisher-Shannon method (VIGNAT; BERCHER, 2003), introduced to jointly quantify the local and global properties of the probability density function of unidimensional signals, is applied in the context of soil complexity. In the current study, the “signals” are represented by a 790x790 set of 1D vertical lines of 790 greyscale values in X-ray CT scan images of soil samples from a sugarcane field and a nearby Atlantic Forest site in northeastern Brazil. For each image and each of these sequences, we calculate Shannon entropy power (SEP) and Fisher information measure (FIM) that quantify the disorder and structural organization of the signal's variation (MARTIN; PENNINI; PLASTINO, 1999). The joint FIM/SEP analysis is then performed through the Fisher-Shannon information plane (FS) through an innovative

normalization procedure to achieve a 91.7% level of accuracy of distinction between the sugarcane plantation and the Atlantic Forest samples.

3.3 Methodology

3.3.1 Soil samples

Twenty-four soil samples analyzed in this work were collected from sugarcane cultivation and a nearby native Atlantic Forest in the northeastern Brazilian region, Pernambuco. The site is between latitudes -7.84836 -7.83519, and longitudes -34.9973 and -34.9935, as shown in figure 1. Two samples were collected at each site, at 10cm and 20cm depth.

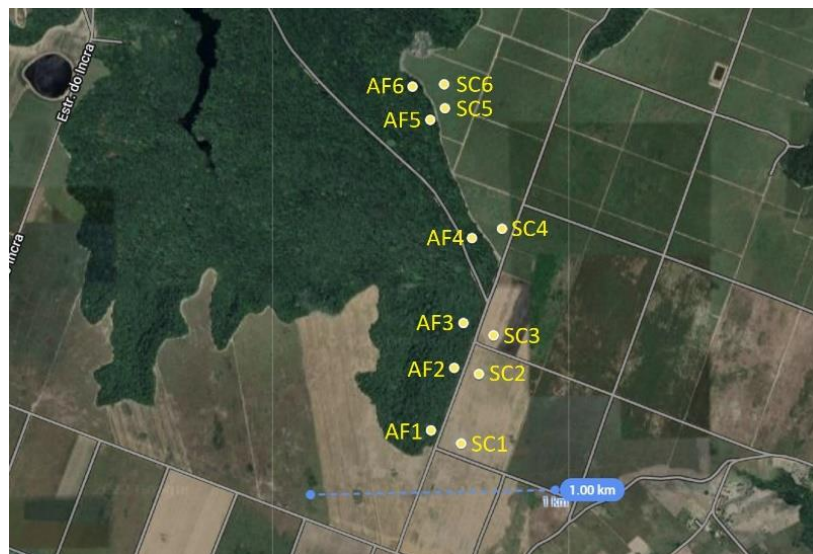


Figure 1. Spatial distribution of sample sites, two samples were taken at each site, at 10 and 20cm depth.

The samples were collected using a soil auger with an internal PVC cylinder of 7.5cm height and 7.5cm diameter, excavated by careful penetration with a cylinder coupled with a blade. After the insertion of the auger in the soil, the cylinders were carefully extracted to ensure the preservation of the original structure of the environment inside the PVC cylinders. The samples were then dried at 40°C to remove the water content before the scanning tomography of the samples.

The CT tomography was performed using a third-generation Nikon XT H 225 ST X-ray microtomography with 150kV voltage, 180 μ A current, 500ms exposure time, and a 45 μ m resolution for voxels. A copper filter with a thickness of 0.5 mm was used to minimize low-intensity photons. After scanning the total cylinder volume in the initial acquisition, a sub-volume of interest was defined and reconstructed using CTPro 3D XT 3.0.3 (Nikon Metrology NV) software. The central part of the cylinder was highlighted to avoid edge influence. The reconstructed 2D axial projections maintained the spatial resolution of the acquisition of 45 μ m and were saved at a radiometric resolution (grayscale level) of 16 bits. The final volume was 790 stacks with 790 x 790 pixels, with an end volume of 790³= 493,039,000 voxels.

The voxel values of the CT scan images correspond to the local sample density. Considering the vertical (gravity) direction as naturally preferential from a phenomenological point of view, we perform calculations on 790x790=624,100 vertical lines of 790 grey-level values each for every sample.

3.3.2 The Fisher-Shannon method

The Fisher-Shannon method consists of a joint analysis of Fisher information measure (FIM), which quantifies the amount of organization (or order) in a signal, and Shannon entropy (SE) which quantifies the amount of disorder (VIGNAT; BERCHER, 2003). Fisher introduced the FIM concept in the statistical theory estimation (FISHER, 1925). It was subsequently used to describe physical systems (ESTAÑÓN *et al.*, 2020; FRIEDEN, 1990), as well as for time series analysis in geophysics (MORENO-TORRES *et al.*, 2018; SULEIMANOV; GUSEINOVA, 2019), ecology (BA *et al.*, 2020), astrophysics (LOVALLO; TELESCA, 2011), meteorology (PIERINI *et al.*, 2016; STOSIC; TELESCA; STOSIC, 2021), hydrology (DA SILVA *et al.*, 2021) and social science (LI *et al.*, 2020).

For a continuous one-dimensional variable X with probability density function (PDF) $f(x)$, the Fisher information measure I_x is defined as (LI *et al.*, 2020)

$$I_x = \int_{-\infty}^{\infty} \left(\frac{\partial}{\partial x} f(x) \right)^2 \frac{1}{f(x)} dx \quad , \quad (1)$$

and Shannon entropy H_x as

$$H_x = - \int_{-\infty}^{\infty} f(x) \log f(x) dx \quad . \quad (2)$$

The Fisher information measure thus describes the local properties of the PDF, while the Shannon entropy describes its global properties (LI *et al.*, 2020). The shape of the PDF is reflected in these measures, as the FIM assumes high values if the PDF is narrow and low values if the PDF is broad, while SE attains high values for a broad PDF and low values for a narrow PDF.

Instead of Shannon entropy, it is often more convenient (ANGULO; ANTOLÍN; SEN, 2008) to use the quantity called Shannon entropy power (SEP), defined by

$$N_x = \frac{1}{2\pi e} e^{2H_x} \quad . \quad (3)$$

The product $C_x = N_x \cdot I_x$ satisfies “isoperimetric inequality” $N_x \cdot I_x \geq 1$ (where equality holds for the Normal distribution), demonstrating that FIM and Shannon entropy are intrinsically related and can be jointly used to characterize the non-stationary behavior of complex signals. The product $N_x I_x$ is called Fisher Shannon complexity (FSC) and can be used as the statistical measure of complexity of the signal under study (DEMBO; COVER; THOMAS, 1991). The joint FIM/SEP analysis is performed through the Fisher Shannon information plane (FS), where Shannon entropy power N_x is used for the horizontal axes, and Fisher information measure I_x is taken for the vertical axis variable (VIGNAT; BERCHER, 2003). The signal is mapped to the point with coordinates (N_x, I_x) which can lie anywhere in the FS plane where the “isoperimetric inequality” $N_x I_x \geq 1$ is satisfied. The distance from the “isocomplexity” line $N_x I_x = 1$ can be used as a measure of the complexity of the signal (LI *et al.*, 2020).

As the above measures depend only on the PDF, Fisher-Shannon analysis can be implemented for real-world datasets corresponding to complex systems through nonparametric density estimation, avoiding parametric assumptions on the distribution.

One possibility is using histograms with the discretized version of (1) and (2). However, in this work, we implement kernel density estimation, which is more reliable (TELESCA; LOVALLO, 2017) in the current case. The Kernel density estimator of the PDF is given by (RAYKAR; DURAISWAMI, 2006)

$$\hat{f}_M(x) = \frac{1}{Nb} \sum_{i=1}^N k\left(\frac{x-x_i}{b}\right) \quad , \quad (4)$$

where $b > 0$ is the so-called bandwidth parameter, N is the length of the signal, and $K(u)$ is the kernel function, a continuous symmetric function that satisfies $K(u) \geq 0$ and $\int_{-\infty}^{+\infty} K(u)du = 1$. The most widely used is the Gaussian kernel $k(u) = (2\pi)^{-1/2} \exp(-u^2/2)$ yielding

$$\hat{f}_M(x) = \frac{1}{Nb\sqrt{2\pi}} \sum_{i=1}^N e^{-\frac{(x-x_i)^2}{2b^2}} \quad . \quad (5)$$

3.4 Results and discussion

The I_x , N_x and C_x values were calculated for each of the 624,100 vertical lines of length 790 for all the 24 CT scan images and for the 790 horizontal planes of $790 \times 790 = 624,100$ voxels each, and for the full $790^3 = 493,039,000$ voxel images. After extensive testing with different combinations of quantities and distribution measures that can be extracted from these calculations, we have found that the first option of considering the set of vertical lines for each sample yields the best distinction between the sugar cane and the Atlantic Forest samples. The descriptive statistics (minimum, maximum, quartiles, mean, and standard deviation) of the I_x , N_x and C_x values of vertical lines are presented in Tables I, II and III, respectively, and the distribution of the values in the 790×790 plane for all samples are presented in Figs. 2, 3 and 4.

Table 1. Descriptive Statistics of Fisher Information Measure I_x .

	min	Q1	Q2	Q3	max	mean	stdev
Atlantic forest							
AF1-10	4.24E-06	6.07E-06	6.50E-06	7.01E-06	1.62E-05	6.62E-06	8.67E-07
AF2-10	3.53E-06	6.79E-06	7.52E-06	8.40E-06	1.76E-05	7.70E-06	1.29E-06
AF3-10	3.65E-06	6.28E-06	6.89E-06	7.64E-06	1.79E-05	7.05E-06	1.09E-06
AF4-10	3.31E-06	6.54E-06	7.14E-06	7.89E-06	1.69E-05	7.34E-06	1.19E-06
AF5-10	4.13E-06	7.13E-06	7.90E-06	8.81E-06	2.02E-05	8.08E-06	1.36E-06
AF6-10	3.79E-06	9.58E-06	1.07E-05	1.19E-05	2.59E-05	1.08E-05	1.86E-06
AF1-20	4.51E-06	7.46E-06	8.14E-06	8.86E-06	1.46E-05	8.20E-06	1.03E-06
AF2-20	3.32E-06	8.10E-06	9.02E-06	1.01E-05	1.78E-05	9.15E-06	1.47E-06
AF3-20	3.45E-06	7.63E-06	8.37E-06	9.20E-06	1.74E-05	8.47E-06	1.19E-06
AF4-20	3.93E-06	7.47E-06	8.20E-06	9.04E-06	1.58E-05	8.31E-06	1.18E-06
AF5-20	3.69E-06	7.33E-06	8.18E-06	9.21E-06	1.82E-05	8.37E-06	1.50E-06
AF6-20	4.08E-06	8.11E-06	9.08E-06	1.02E-05	1.82E-05	9.22E-06	1.54E-06
Sugarcane							
SC1-10	4.91E-06	8.15E-06	8.76E-06	9.40E-06	1.45E-05	8.80E-06	9.37E-07
SC2-10	3.24E-06	8.35E-06	9.35E-06	1.05E-05	2.02E-05	9.47E-06	1.60E-06
SC3-10	3.57E-06	9.05E-06	9.78E-06	1.05E-05	1.61E-05	9.81E-06	1.13E-06
SC4-10	4.52E-06	9.02E-06	9.77E-06	1.06E-05	1.71E-05	9.83E-06	1.16E-06
SC5-10	4.01E-06	9.22E-06	1.01E-05	1.10E-05	1.82E-05	1.01E-05	1.31E-06
SC6-10	3.67E-06	1.07E-05	1.17E-05	1.27E-05	1.94E-05	1.17E-05	1.45E-06
SC1-20	5.11E-06	1.03E-05	1.11E-05	1.19E-05	1.72E-05	1.11E-05	1.15E-06
SC2-20	3.51E-06	8.54E-06	9.36E-06	1.02E-05	1.81E-05	9.43E-06	1.30E-06
SC3-20	3.46E-06	9.87E-06	1.07E-05	1.15E-05	1.78E-05	1.07E-05	1.24E-06
SC4-20	3.96E-06	7.93E-06	8.71E-06	9.57E-06	1.72E-05	8.81E-06	1.26E-06
SC5-20	3.71E-06	9.17E-06	1.01E-05	1.11E-05	1.79E-05	1.01E-05	1.43E-06
SC6-20	6.56E-06	1.27E-05	1.41E-05	1.56E-05	2.68E-05	1.42E-05	2.17E-06

Table 2. Descriptive Statistics of Shannon entropy power N_x .

	min	Q1	Q2	Q3	max	mean	stdev
Atlantic forest							
AF1-10	1.24E+05	2.14E+05	2.37E+05	2.62E+05	4.10E+05	2.39E+05	3.53E+04
AF2-10	7.07E+04	1.84E+05	2.11E+05	2.39E+05	6.14E+05	2.13E+05	4.03E+04
AF3-10	7.43E+04	1.92E+05	2.17E+05	2.44E+05	6.00E+05	2.20E+05	3.99E+04
AF4-10	9.73E+04	1.85E+05	2.09E+05	2.37E+05	6.23E+05	2.15E+05	4.63E+04
AF5-10	8.54E+04	1.76E+05	2.03E+05	2.34E+05	3.88E+05	2.06E+05	4.05E+04
AF6-10	5.55E+04	1.04E+05	1.30E+05	1.65E+05	4.34E+05	1.38E+05	4.11E+04
AF1-20	7.64E+04	1.30E+05	1.45E+05	1.62E+05	3.72E+05	1.48E+05	2.40E+04
AF2-20	6.30E+04	1.22E+05	1.39E+05	1.60E+05	7.27E+05	1.43E+05	3.08E+04
AF3-20	5.92E+04	1.25E+05	1.41E+05	1.58E+05	9.73E+05	1.44E+05	2.84E+04
AF4-20	7.90E+04	1.40E+05	1.58E+05	1.82E+05	3.96E+05	1.64E+05	3.44E+04
AF5-20	6.98E+04	1.47E+05	1.72E+05	2.03E+05	5.56E+05	1.78E+05	4.29E+04
AF6-20	5.91E+04	1.18E+05	1.36E+05	1.58E+05	5.51E+05	1.39E+05	2.98E+04
Sugarcane							
SC1-10	7.31E+04	1.19E+05	1.29E+05	1.41E+05	3.03E+05	1.31E+05	1.71E+04
SC2-10	6.34E+04	1.40E+05	1.72E+05	2.13E+05	9.73E+05	1.79E+05	5.13E+04
SC3-10	6.82E+04	1.06E+05	1.16E+05	1.29E+05	8.74E+05	1.20E+05	2.02E+04
SC4-10	6.50E+04	1.05E+05	1.15E+05	1.28E+05	4.23E+05	1.17E+05	1.82E+04
SC5-10	6.23E+04	1.02E+05	1.14E+05	1.31E+05	4.34E+05	1.20E+05	2.60E+04
SC6-10	5.43E+04	8.70E+04	9.63E+04	1.08E+05	7.01E+05	9.86E+04	1.63E+04
SC1-20	6.05E+04	9.01E+04	9.72E+04	1.05E+05	3.58E+05	9.84E+04	1.22E+04
SC2-20	5.79E+04	1.12E+05	1.26E+05	1.43E+05	1.05E+06	1.30E+05	2.68E+04
SC3-20	5.88E+04	9.36E+04	1.02E+05	1.12E+05	1.10E+06	1.04E+05	1.54E+04
SC4-20	6.46E+04	1.24E+05	1.39E+05	1.57E+05	4.46E+05	1.43E+05	2.69E+04
SC5-20	5.79E+04	1.00E+05	1.12E+05	1.27E+05	5.15E+05	1.17E+05	2.52E+04
SC6-20	3.83E+04	7.48E+04	8.49E+04	9.66E+04	2.19E+05	8.69E+04	1.72E+04

Table 3. Descriptive Statistics of Fisher-Shannon complexity C_x .

	min	Q1	Q2	Q3	max	mean	stdev
Atlantic forest							
AF1-10	1.05E+00	1.36E+00	1.51E+00	1.72E+00	4.30E+00	1.58E+00	3.22E-01
AF2-10	1.02E+00	1.36E+00	1.53E+00	1.79E+00	4.61E+00	1.63E+00	3.89E-01
AF3-10	1.03E+00	1.33E+00	1.46E+00	1.65E+00	4.13E+00	1.54E+00	3.11E-01
AF4-10	1.03E+00	1.30E+00	1.44E+00	1.68E+00	5.08E+00	1.58E+00	4.53E-01
AF5-10	1.02E+00	1.35E+00	1.54E+00	1.84E+00	4.69E+00	1.65E+00	4.22E-01
AF6-10	1.01E+00	1.14E+00	1.32E+00	1.64E+00	5.48E+00	1.47E+00	4.74E-01
AF1-20	1.01E+00	1.12E+00	1.17E+00	1.24E+00	2.29E+00	1.19E+00	1.00E-01
AF2-20	1.01E+00	1.14E+00	1.21E+00	1.33E+00	4.13E+00	1.29E+00	2.69E-01
AF3-20	1.01E+00	1.11E+00	1.16E+00	1.23E+00	4.13E+00	1.20E+00	1.61E-01
AF4-20	1.01E+00	1.18E+00	1.27E+00	1.40E+00	3.58E+00	1.34E+00	2.55E-01
AF5-20	1.01E+00	1.22E+00	1.34E+00	1.55E+00	4.85E+00	1.47E+00	4.17E-01
AF6-20	1.01E+00	1.13E+00	1.21E+00	1.31E+00	2.71E+00	1.25E+00	1.68E-01
Sugarcane							
SC1-10	1.01E+00	1.09E+00	1.12E+00	1.17E+00	2.00E+00	1.14E+00	7.35E-02
SC2-10	1.01E+00	1.29E+00	1.50E+00	1.91E+00	4.44E+00	1.68E+00	5.32E-01
SC3-10	1.01E+00	1.08E+00	1.12E+00	1.20E+00	3.55E+00	1.16E+00	1.19E-01
SC4-10	1.01E+00	1.08E+00	1.11E+00	1.17E+00	2.38E+00	1.14E+00	9.14E-02
SC5-10	1.01E+00	1.08E+00	1.12E+00	1.21E+00	3.79E+00	1.19E+00	2.29E-01
SC6-10	1.00E+00	1.07E+00	1.11E+00	1.17E+00	2.87E+00	1.14E+00	1.02E-01
SC1-20	1.00E+00	1.05E+00	1.07E+00	1.10E+00	1.97E+00	1.08E+00	5.51E-02
SC2-20	1.01E+00	1.10E+00	1.16E+00	1.25E+00	4.03E+00	1.20E+00	1.43E-01
SC3-20	1.01E+00	1.05E+00	1.08E+00	1.12E+00	4.82E+00	1.10E+00	6.40E-02
SC4-20	1.01E+00	1.14E+00	1.20E+00	1.28E+00	3.19E+00	1.23E+00	1.34E-01
SC5-20	1.01E+00	1.08E+00	1.12E+00	1.19E+00	3.36E+00	1.15E+00	1.27E-01
SC6-20	1.00E+00	1.11E+00	1.18E+00	1.27E+00	2.73E+00	1.20E+00	1.28E-01

In order to address the distance from the iso-complexity line $N_x I_x = 1$ as a measure of the complexity of the vertical sample lines (LI *et al.*, 2020), it should be noted that the scales of Shannon entropy power with an average of $\langle N_x \rangle = 1.497 \times 10^5$ and Fisher Information with average $\langle I_x \rangle = 9.307 \times 10^{-6}$ differ in orders of magnitude, while the average the Fisher-Shannon complexity $\langle C_x \rangle = 1.317$ is of the order of unity. If the projection of a point (N_x, I_x) in the FS plane presented in figure 5a to the nearest point on the “isocomplexity” line is denoted by (N_{x0}, I_{x0}) , then the displacement of Shannon Information $\Delta I_x \equiv I_x - I_{x0}$ turns negligible in comparison with the displacement of Shannon entropy power $\Delta N_x \equiv N_x - N_{x0}$, and by minimizing the distance to the iso-complexity line, the points are projected vertically down to the isocomplexity line, and the Euclidean distance is practically reduced to ΔN_x , with no influence of ΔI_x .

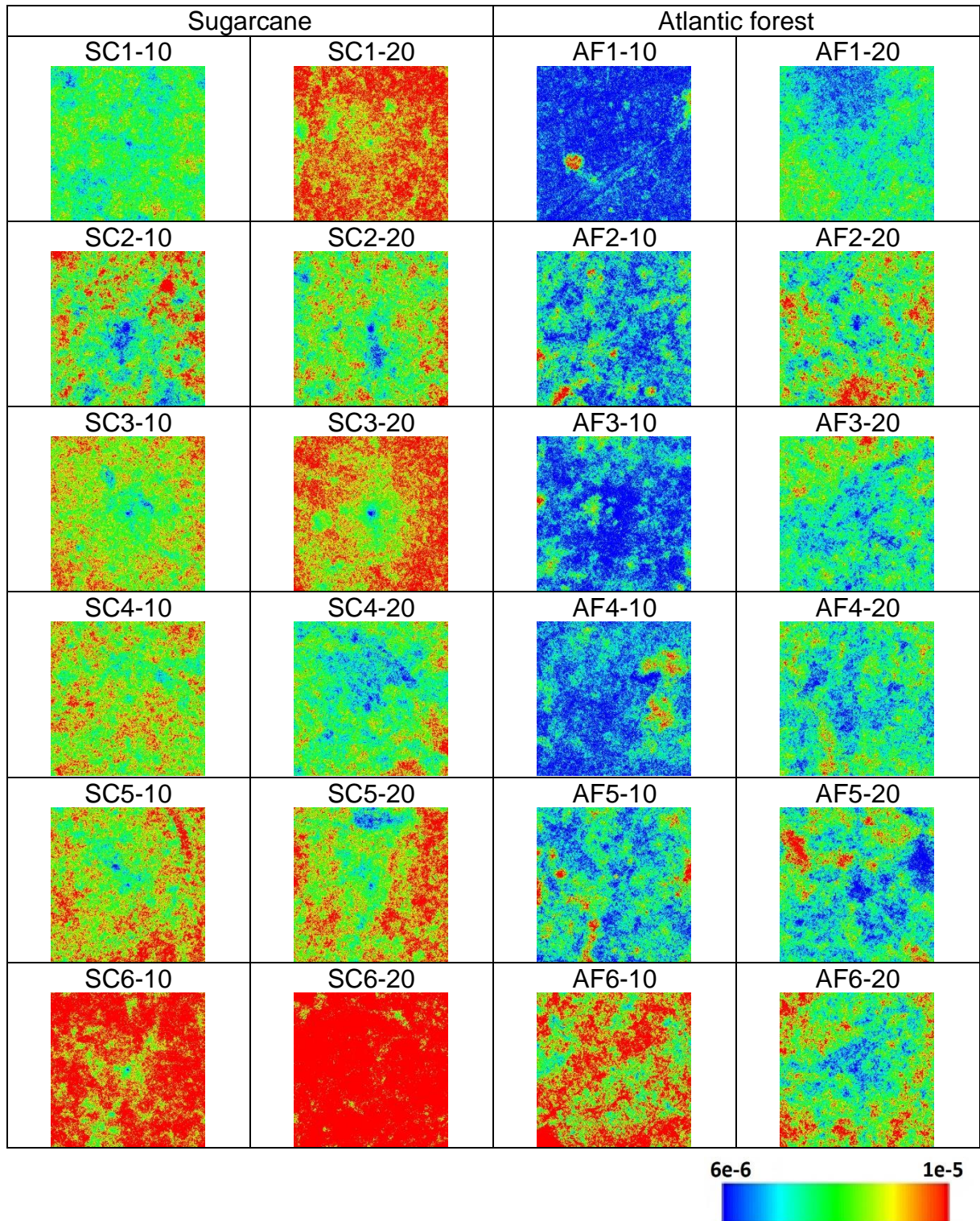


Figure 2. Spatial distribution of the I_x values in the horizontal projection plane for each sample. Pixels are colour-coded in blue below two standard deviations from the global average and red for values above two standard deviations. A spectrum of colors is used for values in between, as per the colour bar.

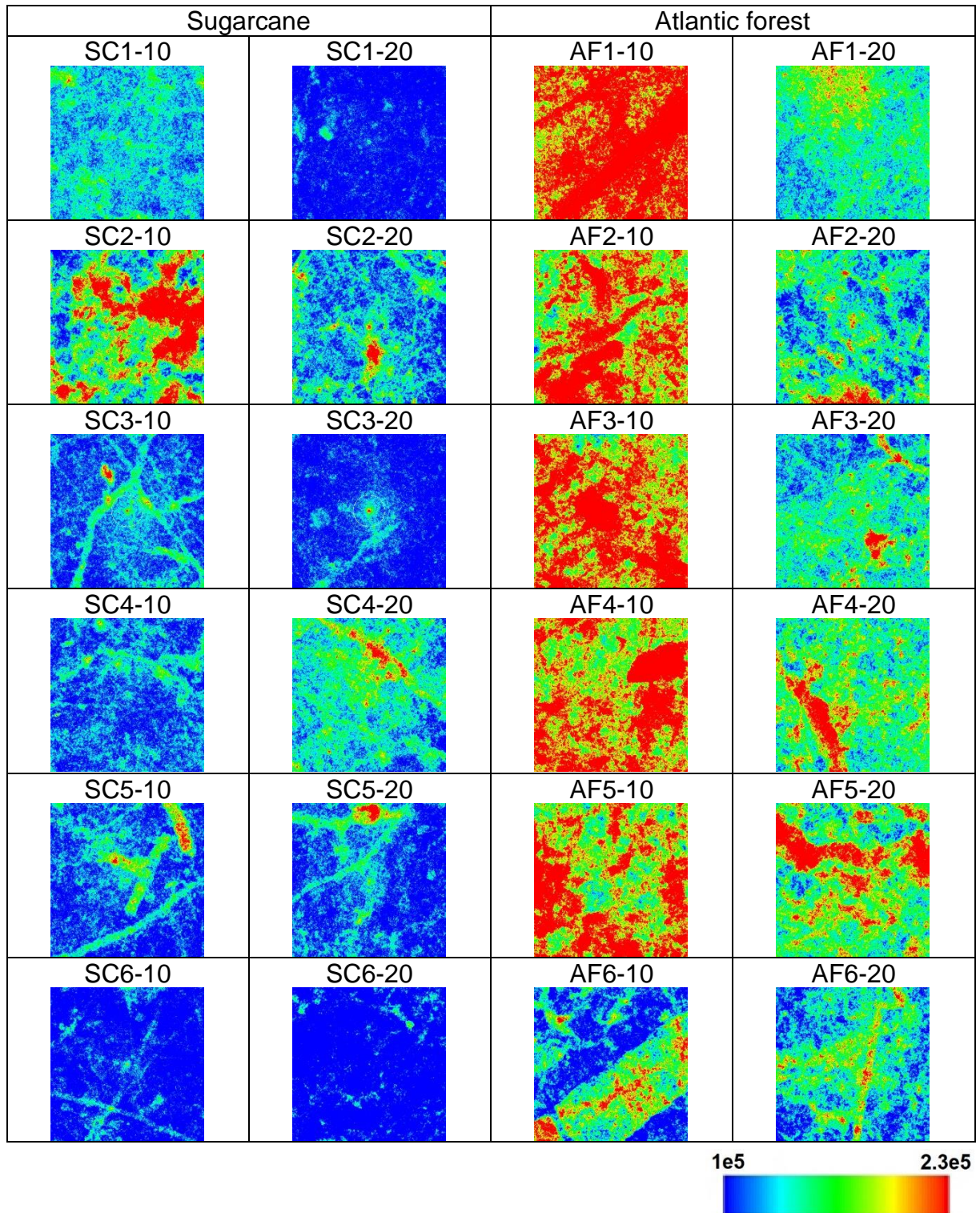


Figure 3. Spatial distribution of the N_x values in the horizontal projection plane for each sample. Pixels are colour-coded in blue below two standard deviations from the global average and red for values above two standard deviations. A spectrum of colors is used for values in between, as per the colour bar.

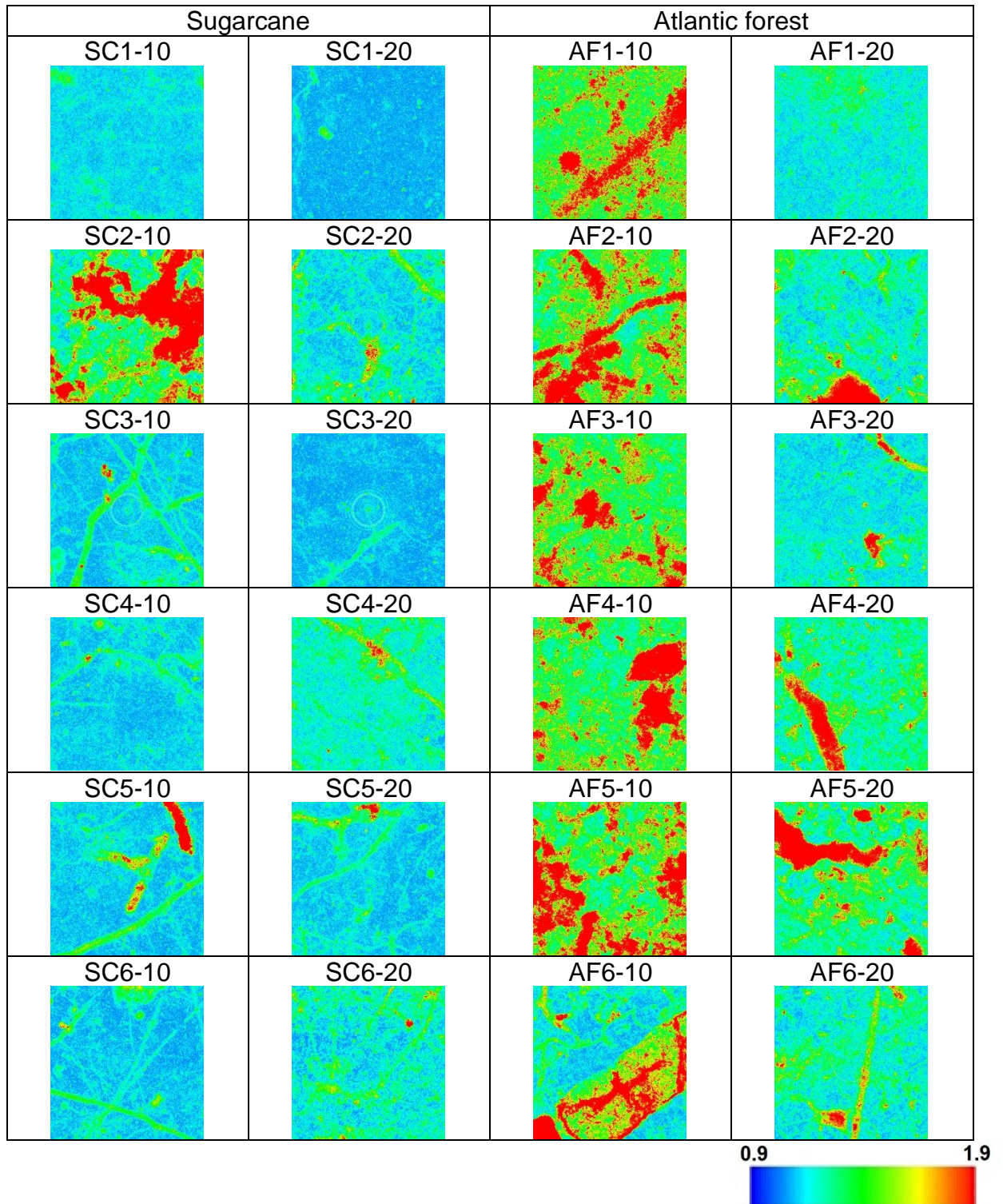


Figure 4. Spatial distribution of the C_x values in the horizontal projection plane for each sample. Pixels are colour-coded in blue below two standard deviations from the global average and red for values above two standard deviations. A spectrum of colors is used for values in between, as per the colour bar.

To mitigate this fact, here we introduce a novel normalization procedure for the variables N_X and I_X . More precisely, first, we identify the maximum value N_{Xmax} among all the samples, and we scale all the sample values as $N'_X = N_X/N_{Xmax}$ and $I'_X = I_X/N_{Xmax}$, thus **preserving** the $C_x \equiv N_X I_X$ complexity values. Distance from a point (N'_X, I'_X) to a projection point (N'_{Xl}, I'_{Xl}) on the isocomplexity plane is now given by

$$d = \sqrt{(N'_X - N'_{Xl})^2 + \left(I'_X - \frac{1}{N'_{Xl}}\right)^2} \quad , \quad (6)$$

and setting the derivative of d concerning N'_{Xl} to zero to find the closest point (N'_{X0}, I'_{X0}) yields the fourth-order polynomial expression for $x \equiv N'_{X0} \equiv 1/I'_{X0}$

$$x^4 - x^3 N'_X + x I'_X - 1 = 0 \quad , \quad (7)$$

which is solved numerically for all samples. The results of this novel procedure are presented in figure 5b, and the distances scatterplot from the iso-complexity plane is presented in figure 6.

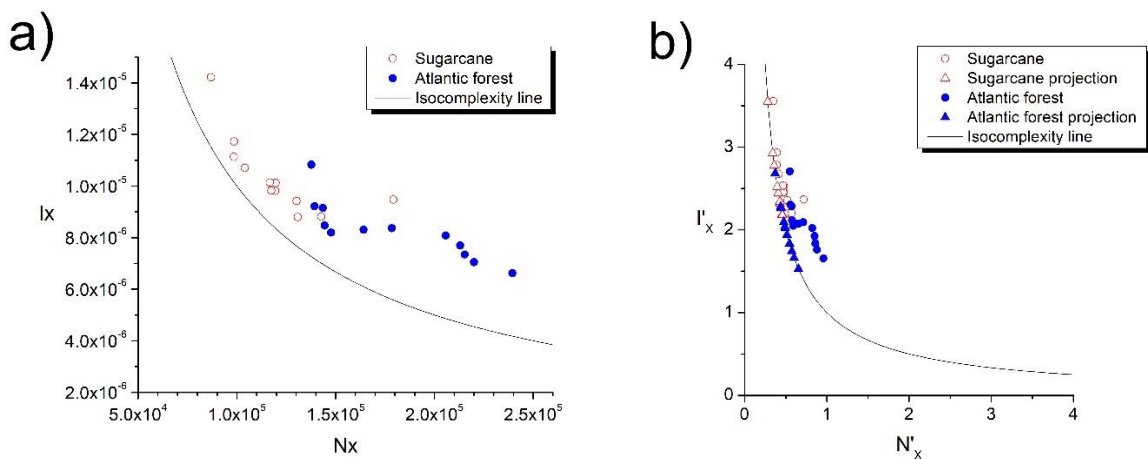


Figure 5 a) Scatterplot of the original (N_X, I_X) value pairs, and b) a scatterplot of the normalized values (N'_X, I'_X) , together with projections (N'_{X0}, I'_{X0}) to the closest point on the iso-complexity line.

The Sugarcane sample's complexity, quantified by the distance from the iso-complexity line (figures 4 and 5), is generally lower than those of the Atlantic Forest samples, exhibiting large fluctuations between the alternative values from samples taken at 10cm and 20cm depth. The complexity values are presented in Table IV.

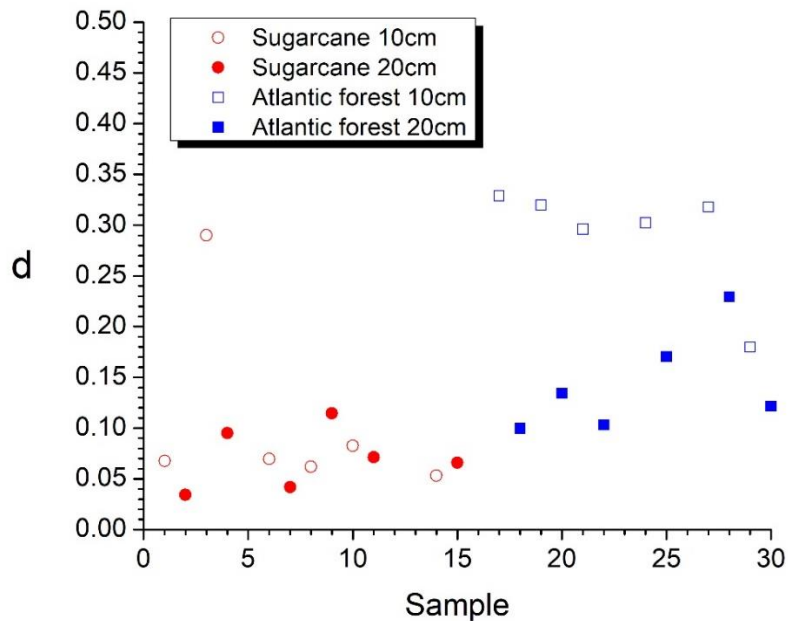


Figure 6 The distances scatterplot from the iso-complexity line, in the order of samples from south to north.

Table 4. Complexity (distance from the isocomplexity plane).

Sugarcane					
SC1-10	SC2-10	SC3-10	SC4-10	SC5-10	SC6-10
0.0676	0.2899	0.0696	0.0619	0.0825	0.0531
SC1-20	SC2-20	SC3-20	SC4-20	SC5-20	SC6-20
0.0342	0.0951	0.0420	0.1144	0.0714	0.0660
Atlantic forest					
AF1-10	AF2-10	AF3-10	AF4-10	AF5-10	AF6-10
0.3290	0.3198	0.2961	0.3022	0.3179	0.1799
AF1-20	AF2-20	AF3-20	AF4-20	AF5-20	AF6-20
0.0998	0.1341	0.1032	0.1704	0.2294	0.1215

To demonstrate the validity of this novel approach, we show in figure 7 the 3D images of the two samples with the lowest and highest complexity, respectively.

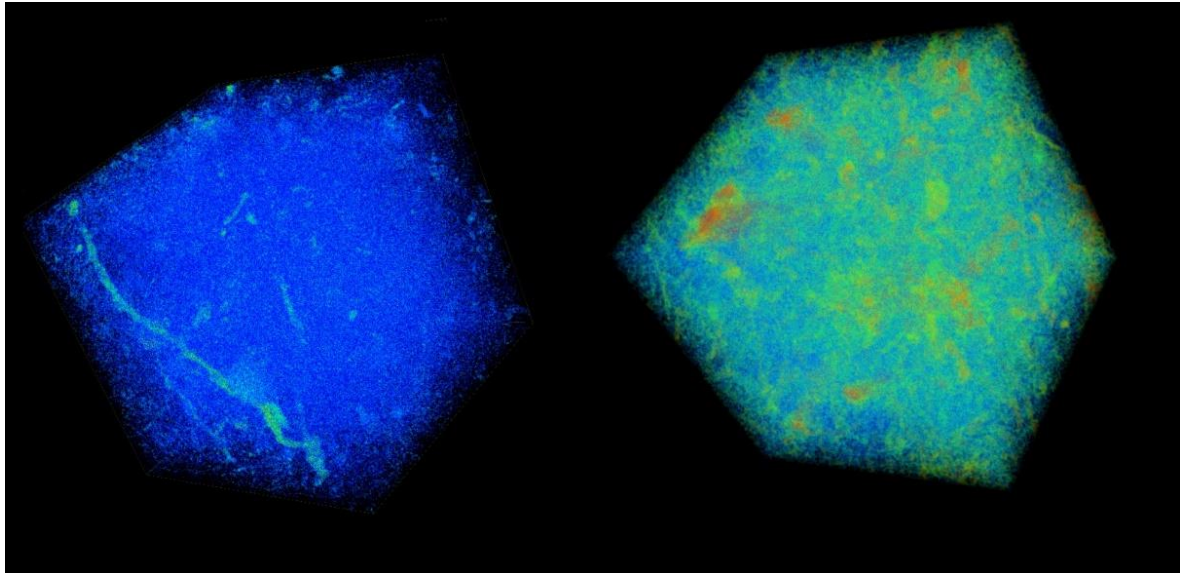


Figure 7. Samples SC1_20 with $d=0.0342$ (left), and AF1_10 with $d=0.329$ (right), at a threshold of 1500 Hounsfield units.

The current approach, without arbitrary parameters (e.g., threshold), yields results that agree well with a visual observation (as seen in figure 5) and provides a precise quantitative measure of the samples' complexity. The usefulness of this approach for quantifying soil degradation should be tested in future studies in the natural environment and controlled laboratory experiments.

Finally, to test the discriminative power of the current approach, we implement here the fitting of values from table 4 to a logistic function, where a categorical variable of zero value is attributed to the sugarcane samples and unit value to the Atlantic Forest samples, with results shown in figure 8.

Considering logistic regression as a binary classifier, the threshold of $d=0.0952$ separates the two groups of samples, with only two samples (SC2-10 and SC4-20) falling into the wrong category. It should be noted here that the k-means method does not produce meaningful results in this case because of the difference in the variance of the d values of the two groups, which is much smaller for the sugarcane samples than for the Atlantic Forest samples.

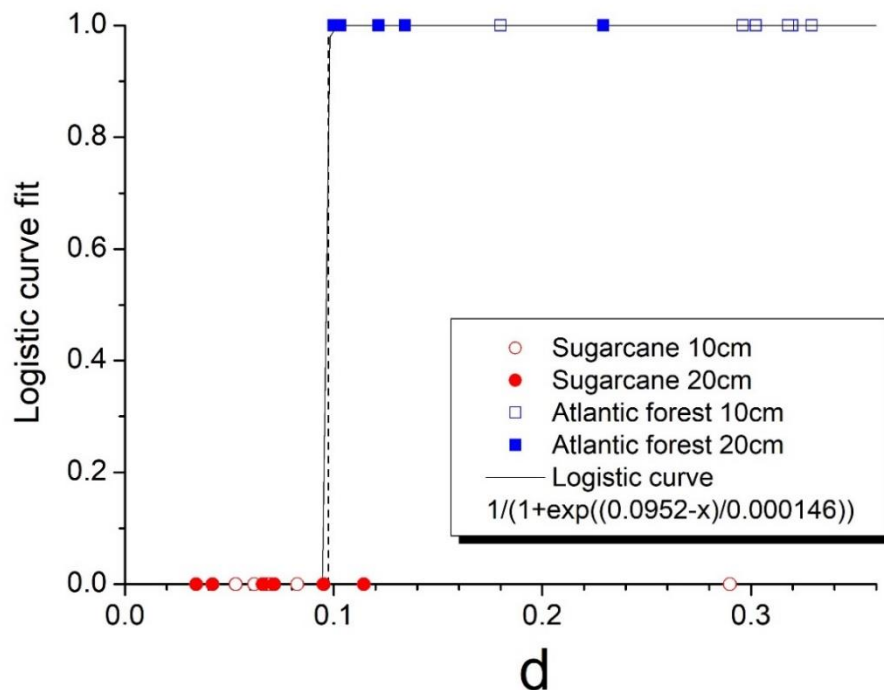


Figure 8. Fit to a logistic function. The vertical dashed line represents the threshold $d = 0.0952$.

Observing the images of I_x , N_x and C_x of the spatial distribution of these samples in Figs. 2, 3 and 4 reveals that the origin of the strikingly high value of $d = 0.290$ for sample SC2-10 stems from the pronounced values of Shannon entropy power N_x . This entropy, in combination with Information, measures values I_x yield Fisher-Shannon complexity C_x for each of the 624,100 vertical lines, somewhat similar to those of the Atlantic Forest samples. Therefore, a correct grouping of 22 out of 24 samples (91.7%) is attained, demonstrating the power of the current novel nonparametric approach.

3.5 Conclusions

Overall, we can claim that the Fisher-Shannon complexity captures the morphological changes induced by land-use change relatively well. More precisely, the sugarcane field sites lie in an area converted from an Atlantic Forest to a plantation.

The subsequent cultivation activities have brought about changes in the soil morphology. While the results are not entirely consistent regarding depth and/or position, the 91.7% grouping success rate may be considered relatively high, where the discrepancies may be attributed to some yet unknown particularities of these sites.

The approach introduced in the current work does not use arbitrary parameters. It provides a rather precise quantitative complexity measure, which may be seen as a quantifier of soil degradation level. Finally, the novel normalization procedure of variables for representation in the Fisher-Shannon information plane, preserving the Fisher-Shannon complexity, may be helpful for general time series and image analysis.

4. Final considerations

In this work two methods, originally used for the analysis of complex signals, Detrended Fluctuation Analysis (DFA) and Fisher-Shannon method (FS), were applied for the first time in the context of innovative analysis of 3D tomographic images of soil. The methods were adapted for image analysis in general, in this case 3D CT images of soil samples from undisturbed sites covered by Atlantic Forest and sites that undergo soil degradation due to land cover change (replacement of native Atlantic Forest vegetation by sugarcane).

Each 3D image contains $N \times N \times N$ gray level voxel values ($N=790$) so 1D DFA was applied on $N \times N$ vertical lines of length N , 2D DFA on N planes of size $N \times N$ along the vertical direction, and 3D DFA on the whole $N \times N \times N$ dataset. In all cases the values of DFA exponents were found to be smaller than 0.5 indicating antipersistence of local density fluctuations, which are consistently stronger (lower exponent value) for the sugar cane plantation sample, than for the Atlantic Forest.

The FS method was applied on $N \times N$ vertical lines of length N ($N=790$) for 24 3D soil images (12 samples from Atlantic Forest and 12 samples from sugarcane plantation, obtained at 10cm and 20 cm depth). For each vertical line the FS information quantifiers Shannon entropy and Fisher information measure were calculated, and a novel method is introduced here for their proper normalization, preserving the Fisher Shannon complexity. In this way a complexity measure is defined as the distance from the isocomplexity line in the normalized FS plane, which may be seen as a quantifier of soil degradation level. This novel approach resulted in a high grouping success rate (91.7%) between soil covered by native vegetation (Atlantic Forest) and soil that was the subject of degradation process as the consequence of land use change (from native Atlantic Forest to sugarcane cultivation).

To achieve the proposed objectives in this work, two programs were developed in C programming language, one that implements the DFA (1D, 2D, and 3D) and the other that implements the FS method, both suitable for 3D tomographic image data from soil samples. While each image is composed of $790 \times 790 \times 790$ 16-bit voxels, totaling 986,078,000 bytes, on one of the computers used in data processing with an I7-7700HQ 2.80GHz processor with 16 GB of RAM, the processing time for each image in the DFA method was relatively short, approximately 90 seconds. The processing

time for each image using the FS method on the same computer was relatively high, around 5 hours. For this reason, parallel processing of 4 images simultaneously was implemented in the case of the FS method.

The results of this work showed that some methods that are used for the analysis of one-dimensional signals can be adapted for the analysis of 2D and 3D images. The suggestion for future work for investigation of soil degradation by analysis of 3D tomographic images from undisturbed and disturbed sites are the use of Multifractal detrended fluctuation analysis (MFDFA) in its original 1D form and its 2D and 3D generalization. Along the information of persistency of density fluctuations obtained by DFA, MFDFA also provides the information about the dominance of large/small fluctuations and the degree of signal multifractality (through the set of parameters of the multifractal spectrum) and these properties could be used as a “fingerprint” of analyzed images. Other methods such as Visibility Graph and Recurrence Plot (together with Recurrence quantification analysis) that provide the set of quantitative measures that describe signal complexity could also be tested for image analysis in general.

In summary, considering the continuous advent of non-invasive X-ray tomographic methods over the last decades, together with the exponential growth of accessible computer power, the spectrum of techniques from other fields of knowledge (such as complex systems theory, information theory, complex networks and statistical physics) that may be adapted for soil sample analysis is rapidly growing, promising novel complementary insights into the intricate structure of soil. The current work should be therefore understood as a contribution in this direction, where two well-known methods originally used for the analysis of complex signals were adapted for this purpose.

5. Supplementary information

Table 1: Characteristics and coordinates of soil samples.

Sample	Land use	Depth (cm)	Soil type	Latitude	Longitude
AF1-10	Atlantic Forest	10	Spodosol	-7.84791	-34.99660
AF2-10	Atlantic Forest	10	Argisol	-7.84562	-34.99575
AF3-10	Atlantic Forest	10	Spodosol	-7.84396	-34.99542
AF4-10	Atlantic Forest	10	Latosol	-7.84084	-34.99511
AF5-10	Atlantic Forest	10	Latosol	-7.83650	-34.99666
AF6-10	Atlantic Forest	10	Latosol	-7.83527	-34.99729
AF1-20	Atlantic Forest	20	Spodosol	-7.84791	-34.99660
AF2-20	Atlantic Forest	20	Latosol	-7.84562	-34.99575
AF3-20	Atlantic Forest	20	Latosol	-7.84396	-34.99542
AF4-20	Atlantic Forest	20	Latosol	-7.84084	-34.99511
AF5-20	Atlantic Forest	20	Latosol	-7.83650	-34.99666
AF6-20	Atlantic Forest	20	Latosol	-7.83527	-34.99729
SC1-10	Sugarcane	10	Spodosol	-7.84836	-34.99551
SC2-10	Sugarcane	10	Argisol	-7.84583	-34.99483
SC3-10	Sugarcane	10	Spodosol	-7.84441	-34.99428
SC4-10	Sugarcane	10	Latosol	-7.83860	-34.99346
SC5-10	Sugarcane	10	Latosol	-7.83610	-34.99610
SC6-10	Sugarcane	10	Latosol	-7.83519	-34.99612
SC1-20	Sugarcane	20	Spodosol	-7.84836	-34.99551
SC2-20	Sugarcane	20	Argisol	-7.84583	-34.99483
SC3-20	Sugarcane	20	Spodosol	-7.84441	-34.99428
SC4-20	Sugarcane	20	Latosol	-7.83860	-34.99346
SC5-20	Sugarcane	20	Latosol	-7.83610	-34.99610
SC6-20	Sugarcane	20	Latosol	-7.83519	-34.99612

References

- AGUIAR, D.; SANTOS, C. R. dos; MENEZES, R. S. C.; ANTONINO, A. C. D.; STOSIC, B. Detrended fluctuation analysis of three-dimensional data: application to soil x-ray ct scans. **Fractals**, v. 30, n. 03+, 2022. DOI: <https://doi.org/10.1142/S0218348X22500426>.
- ALPATOV, A. V.; VIKHROV, S. P.; GRISHANKINA, N. V. Revealing the surface interface correlations in a-Si:H films by 2D detrended fluctuation analysis. **Semiconductors**, v. 47, n. 3, p. 365–371, 2013. DOI: <https://doi.org/10.1134/S1063782613030020>.
- ALVAREZ-RAMIREZ, J.; IBARRA-VALDEZ, C.; RODRIGUEZ, E.; DAGDUG, L. 1 / f-Noise structures in Pollocks’s drip paintings. **Physica A: Statistical Mechanics and its Applications**, v. 387, n. 1, p. 281–295, 2008. DOI: <https://doi.org/10.1016/j.physa.2007.08.047>.
- ANGULO, J. C.; ANTOLÍN, J.; SEN, K. D. Fisher-Shannon plane and statistical complexity of atoms. **Physics Letters, Section A: General, Atomic and Solid State Physics**, v. 372, n. 5, p. 670–674, 2008. DOI: <https://doi.org/10.1016/j.physleta.2007.07.077>.
- BA, R.; SONG, W.; LOVALLO, M.; LO, S.; TELESKA, L. Analysis of multifractal and organization/order structure in Suomi-NPP VIIRS Normalized Difference Vegetation Index series of wildfire affected and unaffected sites by using the multifractal detrended fluctuation analysis and the Fisher-Shannon analysis. **Entropy**, v. 22, n. 4, p. 1–16, 2020. DOI: <https://doi.org/10.3390/e22040415>.
- BARRERA, E.; GONZALEZ, F.; RODRIGUEZ, E.; ALVAREZ-RAMIREZ, J. Correlation of optical properties with the fractal microstructure of black molybdenum coatings. **Applied Surface Science**, v. 256, n. 6, p. 1756–1763, 2010. DOI: <https://doi.org/10.1016/j.apsusc.2009.09.108>.
- BEZDICEK, D. F.; PAPENDICK, R. I.; LAL, R. Introduction: Importance of soil quality to health and sustainable land management. **Methods for Assessing Soil Quality**, p. 1–8, 2015. DOI: <https://doi.org/10.2136/sssaspecpub49.introduction>.
- BISWAS, A.; ZELEKE, T. B.; SI, B. C. Multifractal detrended fluctuation analysis in examining scaling properties of the spatial patterns of soil water storage. **Nonlinear Processes in Geophysics**, v. 19, n. 2, p. 227–238, 2012. DOI: <https://doi.org/10.5194/npg-19-227-2012>.

- BLOKHINA, I. A.; KORONOVSKII, A. A.; DMITRENKO, A. V.; ELIZAROVA, I. V.; MOISEIKINA, T. V.; TUZHILKIN, M. A.; SEMYACHKINA-GLUSHKOVSKAYA, O. V.; PAVLOV, A. N. Characterization of Anesthesia in Rats from EEG in Terms of Long-Range Correlations. **Diagnostics**, v. 13, n. 3, p. 1–10, 2023. DOI: <https://doi.org/10.3390/diagnostics13030426>.
- BORDONAL, R. de O.; CARVALHO, J. L. N.; LAL, R.; DE FIGUEIREDO, E. B.; DE OLIVEIRA, B. G.; LA SCALA, N. Sustainability of sugarcane production in Brazil. A review. **Agronomy for Sustainable Development**, v. 38, n. 2, p. 1–23, 2018. DOI: <https://doi.org/10.1007/s13593-018-0490-x>.
- BOUNOUA, W.; AFTAB, M. F.; OMLIN, C. W. P. Online detrended fluctuation analysis and improved empirical wavelet transform for real-time oscillations detection in industrial control loops. **Computers and Chemical Engineering**, v. 172, n. January, p. 108173, 2023. DOI: <https://doi.org/10.1016/j.compchemeng.2023.108173>.
- BREUER, L.; PAPEN, H.; BUTTERBACH-BAHL, K. N₂O emission from tropical forest soils of Australia. **Journal of Geophysical Research Atmospheres**, v. 105, n. D21, p. 26353–26367, 2000. DOI: <https://doi.org/10.1029/2000JD900424>.
- CAO, J.; TANG, G.; FANG, X.; LIU, Y.; ZHU, Y.; LI, J.; WAGNER, W. Identification of active gully erosion sites in the loess plateau of China using MF-DFA. **Remote Sensing**, v. 12, n. 3, p. 1–21, 2020. DOI: <https://doi.org/10.3390/rs12030589>.
- CÁRDENAS, J. P.; SANTIAGO, A.; TARQUIS, A. M.; LOSADA, J. C.; BORONDO, F.; BENITO, R. M. Soil porous system as heterogeneous complex network. **Geoderma**, v. 160, n. 1, p. 13–21, 2010. DOI: <https://doi.org/10.1016/j.geoderma.2010.04.024>.
- CASTIONI, G. A.; CHERUBIN, M. R.; MENANDRO, L. M. S.; SANCHES, G. M.; BORDONAL, R. de O.; BARBOSA, L. C.; FRANCO, H. C. J.; CARVALHO, J. L. N. Soil physical quality response to sugarcane straw removal in Brazil: A multi-approach assessment. **Soil and Tillage Research**, v. 184, n. August, p. 301–309, 2018. DOI: <https://doi.org/10.1016/j.still.2018.08.007>.
- CAVALCANTI, R. Q.; ROLIM, M. M.; DE LIMA, R. P.; TAVARES, U. E.; PEDROSA, E. M. R.; CHERUBIN, M. R. Soil physical changes induced by sugarcane cultivation in the Atlantic Forest biome, northeastern Brazil. **Geoderma**, v. 370, p. 114353, 2020. DOI: <https://doi.org/10.1016/j.geoderma.2020.114353>.
- CHEN, Z.; IVANOV, P. C.; HU, K.; STANLEY, H. E. Effect of nonstationarities on detrended fluctuation analysis. **Physical Review E - Statistical Physics, Plasmas, Fluids, and Related Interdisciplinary Topics**, v. 65, n. 4, p. 15, 2002. DOI: <https://doi.org/10.1103/PhysRevE.65.041107>.

CONAB. **Acompanhamento da safra brasileira de cana-de-açúcar, v. 7 - Safra 2019/20, n. 2 - Segundo levantamento**. Brasília: Companhia Nacional de Abastecimento, 2020. 64 p.

CURRENTI, G.; NEGRO, C. Del; LAPENNA, V.; TELESKA, L. Fluctuation analysis of the hourly time variability of volcano-magnetic signals recorded at Mt. Etna Volcano, Sicily (Italy). **Chaos, Solitons & Fractals**, v. 23, n. 5, p. 1921–1929, 2005. DOI: <https://doi.org/10.1016/j.chaos.2004.07.035>.

DA SILVA, A. S. A.; MENEZES, R. S. C.; TELESKA, L.; STOSIC, B.; STOSIC, T. Fisher Shannon analysis of drought/wetness episodes along a rainfall gradient in Northeast Brazil. **International Journal of Climatology**, v. 41, n. S1, p. E2097–E2110, 2021. DOI: <https://doi.org/10.1002/joc.6834>.

DE LIMA, N. F.; FERNANDES, L. H. S.; JALE, J. S.; DE MATTOS NETO, P. S. G.; STOŠIĆ, T.; STOŠIĆ, B.; FERREIRA, T. A. E. Long-term correlations and cross-correlations in IBovespa and constituent companies. **Physica A: Statistical Mechanics and its Applications**, v. 492, p. 1431–1438, 2018. DOI: <https://doi.org/10.1016/j.physa.2017.11.070>.

DEHESA, J. S. Cramér–Rao, Fisher–Shannon and LMC–Rényi Complexity-like Measures of Multidimensional Hydrogenic Systems with Application to Rydberg States. **Quantum Reports 2023, Vol. 5, Pages 116-137**, v. 5, n. 1, p. 116–137, 9 fev. 2023. DOI: <https://doi.org/10.3390/quantum5010009>.

DEMBO, A.; COVER, T. M.; THOMAS, J. A. Information Theoretic Inequalities. **IEEE Transactions on Information Theory**, v. 37, n. 6, p. 1501–1518, 1991. DOI: <https://doi.org/10.1109/18.104312>.

ESTAÑÓN, C. R.; AQUINO, N.; PUERTAS-CENTENO, D.; DEHESA, J. S. Two-dimensional confined hydrogen: An entropy and complexity approach. **International Journal of Quantum Chemistry**, v. 120, n. 11, p. 29–31, 2020. DOI: <https://doi.org/10.1002/qua.26192>.

FALCONER, R. E.; HOUSTON, A. N.; OTTEN, W.; BAVEYE, P. C. Emergent behavior of soil fungal dynamics: Influence of soil architecture and water distribution. **Soil Science**, v. 177, n. 2, p. 111–119, 2012. DOI: <https://doi.org/10.1097/SS.0b013e318241133a>.

FERNANDES, L. H. S.; DE ARAUJO, F. H. A.; SILVA, J. W. L. an Analysis of the Predictability of Brazilian Inflation Indexes By Information Theory Quantifiers. **Fractals**, v. 30, n. 4, p. 1–9, 2022. DOI: <https://doi.org/10.1142/S0218348X22500979>.

FERREIRA, P. What detrended fluctuation analysis can tell us about NBA results. **Physica A: Statistical Mechanics and its Applications**, v. 500, p. 92–96, 2018. DOI: <https://doi.org/10.1016/j.physa.2018.02.050>.

FISHER, R. A. Theory of Statistical Estimation. **Mathematical Proceedings of the Cambridge Philosophical Society**, v. 22, n. 5, p. 700–725, 1925. DOI: <https://doi.org/10.1017/S0305004100009580>.

FRIEDEN, B. R. Fisher information, disorder, and the equilibrium distributions of physics. **Physical Review A**, v. 41, n. 8, p. 4265–4276, 1990. DOI: <https://doi.org/10.1103/PhysRevA.41.4265>.

FUENTES, N.; GARCIA, A.; GUEVARA, R.; OROFINO, R.; MATEOS, D. M. Complexity of Brain Dynamics as a Correlate of Consciousness in Anaesthetized Monkeys. **Neuroinformatics**, v. 20, n. 4, p. 1041–1054, 2022. DOI: <https://doi.org/10.1007/s12021-022-09586-3>.

FUJII, K.; SHIBATA, M.; KITAJIMA, K.; ICHIE, T.; KITAYAMA, K.; TURNER, B. L. Plant–soil interactions maintain biodiversity and functions of tropical forest ecosystems. **Ecological Research**, v. 33, n. 1, p. 149–160, 2018. DOI: <https://doi.org/10.1007/s11284-017-1511-y>.

GALDOS, M. V.; PIRES, L. F.; COOPER, H. V.; CALONEGO, J. C.; ROSOLEM, C. A.; MOONEY, S. J. Assessing the long-term effects of zero-tillage on the macroporosity of Brazilian soils using X-ray Computed Tomography. **Geoderma**, v. 337, n. November 2018, p. 1126–1135, 2019. DOI: <https://doi.org/10.1016/j.geoderma.2018.11.031>.

GIBSON, J. R.; LIN, H.; BRUNS, M. A. A comparison of fractal analytical methods on 2- and 3-dimensional computed tomographic scans of soil aggregates. **Geoderma**, v. 134, n. 3–4, p. 335–348, 2006. DOI: <https://doi.org/10.1016/j.geoderma.2006.03.052>.

GOLDBERGER, A. L.; AMARAL, L. A. N.; HAUSDORFF, J. M.; IVANOV, P. C.; PENG, C. K.; STANLEY, H. E. Fractal dynamics in physiology: Alterations with disease and aging. **Proceedings of the National Academy of Sciences of the United States of America**, v. 99, n. SUPPL. 1, p. 2466–2472, 2002. DOI: <https://doi.org/10.1073/pnas.012579499>.

GU, G. F.; ZHOU, W. X. Detrended fluctuation analysis for fractals and multifractals in higher dimensions. **Physical Review E - Statistical, Nonlinear, and Soft Matter Physics**, v. 74, n. 6, p. 1–8, 2006. DOI: <https://doi.org/10.1103/PhysRevE.74.061104>.

HARTEMINK, A. E. The definition of soil since the early 1800s. *In: Advances in Agronomy*. [s.l.] Elsevier Inc., 2016. p. 73–126.

HELLIWELL, J. R.; STURROCK, C. J.; GRAYLING, K. M.; TRACY, S. R.; FLAVEL, R. J.; YOUNG, I. M.; WHALLEY, W. R.; MOONEY, S. J. Applications of X-ray computed tomography for examining biophysical interactions and structural development in soil systems: A review. **European Journal of Soil Science**, v. 64, n. 3, p. 279–297, 2013. DOI: <https://doi.org/10.1111/ejss.12028>.

HOUNSFIELD, G. N. Computerized transverse axial scanning (tomography): I. Description of system. **British Journal of Radiology**, v. 46, n. 552, p. 1016–1022, 1973. DOI: <https://doi.org/10.1259/0007-1285-46-552-1016>.

HOUSTON, A. N.; OTTEN, W.; FALCONER, R.; MONGA, O.; BAVEYE, P. C.; HAPCA, S. M. Quantification of the pore size distribution of soils: Assessment of existing software using tomographic and synthetic 3D images. **Geoderma**, v. 299, p. 73–82, 2017. DOI: <https://doi.org/10.1016/j.geoderma.2017.03.025>.

HU, K.; IVANOV, P. C.; CHEN, Z.; CARPENA, P.; STANLEY, H. E. Effect of trends on detrended fluctuation analysis. **Physical Review E - Statistical Physics, Plasmas, Fluids, and Related Interdisciplinary Topics**, v. 64, n. 1, p. 19, 2001. DOI: <https://doi.org/10.1103/PhysRevE.64.011114>.

IBGE. **Contas de ecossistemas : o uso da terra nos biomas brasileiros: 2000-2018**. Rio de Janeiro: Instituto Brasileiro de Geografia e Estatística, 2020. 95 p.

ISLAM, K. R.; WEIL, R. R. Land use effects on soil quality in a tropical forest ecosystem of Bangladesh. **Agriculture, Ecosystems and Environment**, v. 79, n. 1, p. 9–16, 2000. DOI: [https://doi.org/10.1016/S0167-8809\(99\)00145-0](https://doi.org/10.1016/S0167-8809(99)00145-0).

JON, S.; IAIN, M.; HECK, R. J.; PETH, S. **X-ray Imaging of the Soil Porous Architecture**. Cham: Springer International Publishing, 2022.

JUAREZ, S.; NUNAN, N.; DUDAY, A. C.; POUTEAU, V.; SCHMIDT, S.; HAPCA, S.; FALCONER, R.; OTTEN, W.; CHENU, C. Effects of different soil structures on the decomposition of native and added organic carbon. **European Journal of Soil Biology**, v. 58, p. 81–90, 2013. DOI: <https://doi.org/10.1016/j.ejsobi.2013.06.005>.

KANTELHARDT, J. W.; KOSCIELNY-BUNDE, E.; REGO, H. H. A.; HAVLIN, S.; BUNDE, A. Detecting long-range correlations with detrended fluctuation analysis. **Physica A: Statistical Mechanics and its Applications**, v. 295, n. 3–4, p. 441–454, 2001. DOI: [https://doi.org/10.1016/S0378-4371\(01\)00144-3](https://doi.org/10.1016/S0378-4371(01)00144-3).

KATAOKA, T.; MIYAGUCHI, T.; AKIMOTO, T. Detrended fluctuation analysis of earthquake data. **Physical Review Research**, v. 3, n. 3, p. 1–9, 2021. DOI: <https://doi.org/10.1103/PhysRevResearch.3.033081>.

KATUWAL, S.; ARTHUR, E.; TULLER, M.; MOLDRUP, P.; DE JONGE, L. W. Quantification of Soil Pore Network Complexity with X-ray Computed Tomography and Gas Transport Measurements. **Soil Science Society of America Journal**, v. 79, n. 6, p. 1577–1589, 2015. DOI: <https://doi.org/10.2136/sssaj2015.06.0227>.

KIRÁLY, A.; JÁNOSI, I. M. Detrended fluctuation analysis of daily temperature records: Geographic dependence over Australia. **Meteorology and Atmospheric Physics**, v. 88, n. 3–4, p. 119–128, 2005. DOI: <https://doi.org/10.1007/s00703-004-0078-7>.

KRISTOUFEK, L. Are the crude oil markets really becoming more efficient over time? Some new evidence. **Energy Economics**, v. 82, p. 253–263, 2019. DOI: <https://doi.org/10.1016/j.eneco.2018.03.019>.

KWAPIÉ, J.; ATOREK, M. W. ; ZITIS, P. I.; KAKINAKA, S.; UMENO, K.; HANIAS, M. P.; STAVRINIDES, S. G.; POTIRAKIS, S. M. Investigating Dynamical Complexity and Fractal Characteristics of Bitcoin/US Dollar and Euro/US Dollar Exchange Rates around the COVID-19 Outbreak. **Entropy 2023, Vol. 25, Page 214**, v. 25, n. 2, p. 214, 22 jan. 2023. DOI: <https://doi.org/10.3390%2Fe25020214>.

LABRIÈRE, N.; LOCATELLI, B.; LAUMONIER, Y.; FREYCON, V.; BERNOUX, M. Soil erosion in the humid tropics: A systematic quantitative review. **Agriculture, Ecosystems and Environment**, v. 203, p. 127–139, 2015. DOI: <https://doi.org/10.1016/j.agee.2015.01.027>.

LEMENIH, M.; KARLTUN, E.; OLSSON, M. Assessing soil chemical and physical property responses to deforestation and subsequent cultivation in smallholders farming system in Ethiopia. **Agriculture, Ecosystems and Environment**, v. 105, n. 1–2, p. 373–386, 2005. DOI: <https://doi.org/10.1016/j.agee.2004.01.046>.

LI, P.; YU, L.; YANG, J.; LO, M. T.; HU, C.; BUCHMAN, A. S.; BENNETT, D. A.; HU, K. Interaction between the progression of Alzheimer’s disease and fractal degradation. **Neurobiology of Aging**, v. 83, p. 21–30, 2019. DOI: <https://doi.org/10.1016/j.neurobiolaging.2019.08.023>.

LI, X.; TELESKA, L.; LOVALLO, M.; XU, X.; ZHANG, J.; SONG, W. Spectral and informational analysis of pedestrian contact force in simulated overcrowding conditions. **Physica A: Statistical Mechanics and its Applications**, v. 555, p. 124614, 2020. DOI: <https://doi.org/10.1016/j.physa.2020.124614>.

LIU, Q.; HE, W.; GU, B.; JIANG, Y. Detecting abrupt dynamic change based on changes in the fractal properties of spatial images. **Theoretical and Applied Climatology**, v. 130, n. 1–2, p. 435–442, 2017. DOI: <https://doi.org/10.1007/s00704-016-1889-4>.

LIU, W.; CHEN, W.; ZHANG, Z. A Novel Fault Diagnosis Approach for Rolling Bearing Based on High-Order Synchrosqueezing Transform and Detrended Fluctuation Analysis. **IEEE Access**, v. 8, p. 12533–12541, 2020. DOI: <https://doi.org/10.1109/ACCESS.2020.2965744>.

LOVALLO, M.; PIERINI, J. O.; TELESKA, L. Power spectrum and Fisher-Shannon information plane analysis of tidal records. **Physica A: Statistical Mechanics and its Applications**, v. 391, n. 20, p. 4711–4719, 2012. DOI: <https://doi.org/10.1016/j.physa.2012.05.047>.

- LOVALLO, M.; TELESKA, L. Complexity measures and information planes of x-ray astrophysical sources. **Journal of Statistical Mechanics: Theory and Experiment**, v. 2011, n. 3, 2011. DOI: <https://doi.org/10.1088/1742-5468/2011/03/P03029>.
- LUO, L.; LIN, H. Lacunarity and Fractal Analyses of Soil Macropores and Preferential Transport Using Micro-X-Ray Computed Tomography. **Vadose Zone Journal**, v. 8, n. 1, p. 233–241, 2009. DOI: <https://doi.org/10.2136/vzj2008.0010>.
- MAHARJAN, M.; SANALLAH, M.; RAZAVI, B. S.; KUZYAKOV, Y. Effect of land use and management practices on microbial biomass and enzyme activities in subtropical top-and sub-soils. **Applied Soil Ecology**, v. 113, p. 22–28, 2017. DOI: <https://doi.org/10.1016/j.apsoil.2017.01.008>.
- MALLICK, J.; TALUKDAR, S.; ALSUBIH, M.; SALAM, R.; AHMED, M.; KAHLA, N. Ben; SHAMIMUZZAMAN, M. Analysing the trend of rainfall in Asir region of Saudi Arabia using the family of Mann-Kendall tests, innovative trend analysis, and detrended fluctuation analysis. **Theoretical and Applied Climatology**, v. 143, n. 1–2, p. 823–841, 2021. DOI: <https://doi.org/10.1007/s00704-020-03448-1>.
- MARTIN, M. T.; PENNINI, F.; PLASTINO, A. Fisher's information and the analysis of complex signals. **Physics Letters, Section A: General, Atomic and Solid State Physics**, v. 256, n. 2–3, p. 173–180, 1999. DOI: [https://doi.org/10.1016/S0375-9601\(99\)00211-X](https://doi.org/10.1016/S0375-9601(99)00211-X).
- MARTÍNEZ-FLORES, C. Shannon entropy and Fisher information for endohedral confined one- and two-electron atoms. **Physics Letters, Section A: General, Atomic and Solid State Physics**, v. 386, p. 126988, 2021. DOI: <https://doi.org/10.1016/j.physleta.2020.126988>.
- MOHTI, W.; DIONÍSIO, A.; FERREIRA, P.; VIEIRA, I. Frontier markets' efficiency: mutual information and detrended fluctuation analyses. **Journal of Economic Interaction and Coordination**, v. 14, n. 3, p. 551–572, 2019. DOI: <https://doi.org/10.1007/s11403-018-0224-9>.
- MORENO-TORRES, L. R.; GOMEZ-VIEYRA, A.; LOVALLO, M.; RAMÍREZ-ROJAS, A.; TELESKA, L. Investigating the interaction between rough surfaces by using the Fisher–Shannon method: Implications on interaction between tectonic plates. **Physica A: Statistical Mechanics and its Applications**, v. 506, p. 560–565, 2018. DOI: <https://doi.org/10.1016/j.physa.2018.04.023>.
- NIE, Q.; XU, J.; MAN, W.; SUN, F. Detrended fluctuation analysis of spatial patterns on urban impervious surface. **Environmental Earth Sciences**, v. 74, n. 3, p. 2531–2538, 2015. DOI: <https://doi.org/10.1007/s12665-015-4271-4>.

ORTIZ, P. F. S.; ROLIM, M. M.; DE LIMA, J. L. P.; PEDROSA, E. M. R.; DANTAS, M. S. M.; TAVARES, U. E. Physical qualities of an Ultisol under sugarcane and Atlantic forest in Brazil. **Geoderma Regional**, v. 11, p. 62–70, 2017. DOI: <https://doi.org/10.1016/j.geodrs.2017.10.001>.

PENG, C. K.; BULDYREV, S. V.; HAVLIN, S.; SIMONS, M.; STANLEY, H. E.; GOLDBERGER, A. L. Mosaic organization of DNA nucleotides. **Physical Review E**, v. 49, n. 2, p. 1685–1689, 1994. DOI: <https://journals.aps.org/pre/abstract/10.1103/PhysRevE.49.1685>.

PERRET, J. S.; PRASHER, S. O.; KACIMOV, A. R. Mass fractal dimension of soil macropores using computed tomography: From the box-counting to the cube-counting algorithm. **European Journal of Soil Science**, v. 54, n. 3, p. 569–579, 2003. DOI: <https://doi.org/10.1046/j.1365-2389.2003.00546.x>.

PETROVIC, A. M.; SIEBERT, J. E.; RIEKE, P. E. Soil Bulk Density Analysis in Three Dimensions by Computed Tomographic Scanning. **Soil Science Society of America Journal**, v. 46, n. 3, p. 445–450, 1982. DOI: <https://doi.org/10.2136/sssaj1982.03615995004600030001x>.

PIERINI, J. O.; LOVALLO, M.; GÓMEZ, E. A.; TELESCA, L. Fisher–Shannon analysis of the time variability of remotely sensed sea surface temperature at the Brazil–Malvinas Confluence. **Oceanologia**, v. 58, n. 3, p. 187–195, 2016. DOI: <https://doi.org/10.1016/j.oceano.2016.02.003>.

PIRES, L. F.; ROQUE, W. L.; ROSA, J. A.; MOONEY, S. J. 3D analysis of the soil porous architecture under long term contrasting management systems by X-ray computed tomography. **Soil and Tillage Research**, v. 191, p. 197–206, 2019. DOI: <https://doi.org/10.1016/j.still.2019.02.018>.

RABOT, E.; WIESMEIER, M.; SCHLÜTER, S.; VOGEL, H. J. Soil structure as an indicator of soil functions: A review. **Geoderma**, v. 314, n. June 2017, p. 122–137, 2018. DOI: <http://dx.doi.org/10.1016/j.geoderma.2017.11.009>.

RAFIQUE, M.; IQBAL, J.; LONE, K. J.; KEARFOTT, K. J.; RAHMAN, S. U.; HUSSAIN, L. Multifractal detrended fluctuation analysis of soil radon (^{222}Rn) and thoron (^{220}Rn) time series. **Journal of Radioanalytical and Nuclear Chemistry**, v. 328, n. 1, p. 425–434, 2021. DOI: <https://doi.org/10.1007/s10967-021-07650-x>.

RAYKAR, V. C.; DURAISWAMI, R. Fast optimal bandwidth selection for kernel density estimation. **Proceedings of the Sixth SIAM International Conference on Data Mining**, v. 2006, p. 524–528, 2006. DOI: <https://doi.org/10.1137/1.9781611972764.53>.

ROY, A.; PERFECT, E. Lacunarity analyses of multifractal and natural grayscale patterns. **Fractals**, v. 22, n. 3, p. 1–9, 2014. DOI: <https://doi.org/10.1142/S0218348X14400039>.

- SAMEC, M.; SANTIAGO, A.; CÁRDENAS, J. P.; BENITO, R. M.; TARQUIS, A. M.; MOONEY, S. J.; KOROŠAK, D. Quantifying soil complexity using network models of soil porous structure. **Nonlinear Processes in Geophysics**, v. 20, n. 1, p. 41–45, 2013. DOI: <https://doi.org/10.5194/npg-20-41-2013>.
- SAN JOSÉ MARTÍNEZ, F.; MARTÍN, M. A.; CANIEGO, F. J.; TULLER, M.; GUBER, A.; PACHEPSKY, Y.; GARCÍA-GUTIÉRREZ, C. Multifractal analysis of discretized X-ray CT images for the characterization of soil macropore structures. **Geoderma**, v. 156, n. 1–2, p. 32–42, 2010. DOI: <https://doi.org/10.1016/j.geoderma.2010.01.004>.
- SANTOS, C. R. dos; ANTONINO, A. C. D.; HECK, R. J.; LUCENA, L. R. R. de; HOLANDA, A. C. de O.; SILVA, A. S. A. da; STOSIC, B.; MENEZES, R. S. C. 3D Soil Void Space Lacunarity As an Index of Degradation After Land Use Change. **Acta Scientiarum - Agronomy**, v. 42, p. 1–9, 2020. DOI: <https://doi.org/10.4025/actasciagron.v42i1.42941>.
- SCHLÜTER, S.; GROSSMANN, C.; DIEHL, J.; WU, G. M.; TISCHER, S.; DEUBEL, A.; RÜCKNAGEL, J. Long-term effects of conventional and reduced tillage on soil structure, soil ecological and soil hydraulic properties. **Geoderma**, v. 332, n. July, p. 10–19, 2018. DOI: <https://doi.org/10.1016/j.geoderma.2018.07.001>.
- SHANNON, C. E. A mathematical theory of communication. **Bell Syst. Tech**, v. 27, n. 3, p. 379–423, 1948. DOI: <https://doi.org/10.1002/j.1538-7305.1948.tb01338.x>.
- SKORDAS, E. S.; CHRISTOPOULOS, S. R. G.; SARLIS, N. V. Detrended fluctuation analysis of seismicity and order parameter fluctuations before the M7.1 Ridgecrest earthquake. **Natural Hazards**, v. 100, n. 2, p. 697–711, 2020. DOI: <https://doi.org/10.1007/s11069-019-03834-7>.
- SPARKS, D. L. **Environmental Soil Chemistry**. San Diego: Academic Press, 2003.
- STOSIC, B.; AGUIAR, J. D. A.; MENEZES, R.; ANTONINO, A. D.; STOSIC, T.; TARQUIS, A. M. **Quantifying soil complexity using Fisher Information of 3d X-ray CT scan images**. [s.l.: s.n.]. DOI: <https://doi.org/10.5194/egusphere-egu22-13157>.
- STOSIC, T.; TELESKA, L.; STOSIC, B. Multiparametric statistical and dynamical analysis of angular high-frequency wind speed time series. **Physica A: Statistical Mechanics and its Applications**, v. 566, p. 125627, 2021. DOI: <https://doi.org/10.1016/j.physa.2020.125627>.
- SULEIMANOV, B. A.; GUSEINOVA, N. I. Analyzing the State of Oil Field Development Based on the Fisher and Shannon Information Measures. **Automation and Remote Control**, v. 80, n. 5, p. 882–896, 2019. DOI: <https://doi.org/10.1134/S0005117919050072>.

TARQUIS, A. M.; HECK, R. J.; ANDINA, D.; ALVAREZ, A.; ANTÓN, J. M. Pore network complexity and thresholding of 3D soil images. **Ecological Complexity**, v. 6, n. 3, p. 230–239, 2009. DOI: <https://doi.org/10.1016/j.ecocom.2009.05.010>.

TATLI, H.; DALFES, H. N. Long-Time Memory in Drought via Detrended Fluctuation Analysis. **Water Resources Management**, v. 34, n. 3, p. 1199–1212, 2020. DOI: <https://doi.org/10.1007/s11269-020-02493-9>.

TELESCA, L.; AROMANDO, A.; FARIDANI, F.; LOVALLO, M.; CARDETTINI, G.; ABATE, N.; PAPITTO, G.; LASAPONARA, R. Exploring Long-Term Anomalies in the Vegetation Cover of Peri-Urban Parks Using the Fisher-Shannon Method. **Entropy**, v. 24, n. 12, p. 1–17, 2022. DOI: <https://doi.org/10.3390/e24121784>.

TELESCA, L.; LOVALLO, M. On the performance of Fisher Information Measure and Shannon entropy estimators. **Physica A: Statistical Mechanics and its Applications**, v. 484, p. 569–576, 2017. DOI: <https://doi.org/10.1016/j.physa.2017.04.184>.

TELESCA, L.; LOVALLO, M.; ALCAZ, V.; ILIES, I. Site-dependent organization structure of seismic microtremors. **Physica A: Statistical Mechanics and its Applications**, v. 421, p. 541–547, 1 mar. 2015. DOI: <https://doi.org/10.1016/j.physa.2014.11.061>.

TELLES, E. de C. C.; DE CAMARGO, P. B.; MARTINELLI, L. A.; TRUMBORE, S. E.; DA COSTA, E. S.; SANTOS, J.; HIGUCHI, N.; OLIVEIRA, R. C. Influence of soil texture on carbon dynamics and storage potential in tropical forest soils of Amazonia. **Global Biogeochemical Cycles**, v. 17, n. 2, p. n/a-n/a, 2003. DOI: <https://doi.org/10.1029/2002gb001953>.

TORRE, I. G.; LOSADA, J. C.; HECK, R. J.; TARQUIS, A. M. Multifractal analysis of 3D images of tillage soil. **Geoderma**, v. 311, p. 167–174, 2018. DOI: <https://doi.org/10.1016/j.geoderma.2017.02.013>.

TORRE, I. G.; LOSADA, J. C.; TARQUIS, A. M. Multiscaling properties of soil images. **Biosystems Engineering**, v. 168, p. 133–141, 2018. DOI: <https://doi.org/10.1016/j.biosystemseng.2016.11.006>.

TORRE, I. G.; MARTÍN-SOTOCA, J. J.; LOSADA, J. C.; LÓPEZ, P.; TARQUIS, A. M. Scaling properties of binary and greyscale images in the context of X-ray soil tomography. **Geoderma**, v. 365, n. June 2019, p. 114205, 2020. DOI: <https://doi.org/10.1016/j.geoderma.2020.114205>.

VARGAS-OLMOS, C.; MURGUIÁ, J. S.; RAMÍREZ-TORRES, M. T.; MEJÍA CARLOS, M.; ROSU, H. C.; GONZÁLEZ-AGUILAR, H. Two-dimensional DFA scaling analysis applied to encrypted images. **International Journal of Modern Physics C**, v. 26, n. 8, p. 1–12, 2015. DOI: <https://doi.org/10.1142/S012918311550093X>.

VAZ, J. R.; SILVA, L. M.; STERGIIOU, N. Stride-to-Stride Fluctuations of Human Gait Are Affected By Chronobiology: An Exploratory Study. **Advanced Biology**, v. 2200235, p. 1–6, 2023. DOI: <https://doi.org/10.1002/adbi.202200235>.

VELAZQUEZ-CAMILO, O.; BOLAÑOS-REYNOSO, E.; RODRIGUEZ, E.; ALVAREZ-RAMIREZ, J. Fractal analysis of crystallization slurry images. **Journal of Crystal Growth**, v. 312, n. 6, p. 842–850, 2010. DOI: <https://doi.org/10.1016/j.jcrysgro.2009.12.060>.

VIGNAT, C.; BERCHER, J. F. Analysis of signals in the fisher - Shannon information plane. **Physics Letters, Section A: General, Atomic and Solid State Physics**, v. 312, n. 1–2, p. 27–33, 2003. DOI: [https://doi.org/10.1016/S0375-9601\(03\)00570-X](https://doi.org/10.1016/S0375-9601(03)00570-X).

WANG, J.; GUO, L.; BAI, Z.; YANG, L. Using computed tomography (CT) images and multi-fractal theory to quantify the pore distribution of reconstructed soils during ecological restoration in opencast coal-mine. **Ecological Engineering**, v. 92, p. 148–157, 2016. DOI: <https://doi.org/10.1016/j.ecoleng.2016.03.029>.

WANG, M.; XU, S.; KONG, C.; ZHAO, Y.; SHI, X.; GUO, N. Assessing the effects of land use change from rice to vegetable on soil structural quality using X-ray CT. **Soil and Tillage Research**, v. 195, n. April 2016, p. 104343, 2019. DOI: <https://doi.org/10.1016/j.still.2019.104343>.

WILCKE, W.; YASIN, S.; ABRAMOWSKI, U.; VALAREZO, C.; ZECH, W. Nutrient storage and turnover in organic layers under tropical montane rain forest in Ecuador. **European Journal of Soil Science**, v. 53, n. 1, p. 15–27, 2002. DOI: <https://doi.org/10.1046/j.1365-2389.2002.00411.x>.

WOHL, E.; BARROS, A.; BRUNSELL, N.; CHAPPELL, N. A.; COE, M.; GIAMBELLUCA, T.; GOLDSMITH, S.; HARMON, R.; HENDRICKX, J. M. H.; JUVIK, J.; MCDONNELL, J.; OGDEN, F. The hydrology of the humid tropics. **Nature Climate Change**, v. 2, n. 9, p. 655–662, 2012. DOI: <https://doi.org/10.1038/nclimate1556>.

YAMASAKI, K.; MUCHNIK, L.; HAVLIN, S.; BUNDE, A.; STANLEY, H. E. Scaling and memory in volatility return intervals in financial markets. **Proceedings of the National Academy of Sciences of the United States of America**, v. 102, n. 26, p. 9424–9428, 2005. DOI: <https://doi.org/10.1073/pnas.0502613102>.

ZHOU, H.; PENG, X.; PETH, S.; XIAO, T. Q. Effects of vegetation restoration on soil aggregate microstructure quantified with synchrotron-based micro-computed tomography. **Soil and Tillage Research**, v. 124, p. 17–23, 2012. DOI: <https://doi.org/10.1016/j.still.2012.04.006>.

ZHOU, H.; PERFECT, E.; LI, B. G.; LU, Y. Z. Effects of bit depth on the multifractal analysis of grayscale images. **Fractals**, v. 18, n. 1, p. 127–138, 2010. DOI: <https://doi.org/10.1142/S0218348X10004749>.

ZHOU, H.; PERFECT, E.; LU, Y. Z.; LI, B. G.; PENG, X. H. Multifractal analyses of grayscale and binary soil thin section images. **Fractals**, v. 19, n. 3, p. 299–309, 2011. DOI: <https://doi.org/10.1142/S0218348X11005403>.